Fatigue Crack Growth Life Assessment Using 3D Finite Element Analysis

Paulian Catalin Ilie

A Thesis

in

The Department

of

Mechanical and Industrial Engineering

Presented in Partial Fulfillment of the Requirements

For the Degree of

Master of Applied Science (Mechanical Engineering) at

Concordia University

Montreal, Quebec, Canada

March 2022

© Paulian Catalin Ilie, 2022

CONCORDIA UNIVERSITY
School of Graduate Studies

This is to certify that the thesis prepared

By: Paulian Catalin Ilie

Entitled: Fatigue Crack Growth Life Assessment Using 3D Finite Element Analysis

and submitted in partial fulfillment of the requirements for the degree of

Master of Applied Science (Mechanical Engineering)

complies with the regulations of the University and meets the accepted standards with respect to originality and quality.

Signed by the final Examining Committee:

Dr. R. Sedaghati	Chair
Dr. R. Sedaghati	Examiner
Dr. B. Li	Examiner
Dr. A. Loghin	External Examiner
Dr. A. Ince	Supervisor

Approved by _____
Dr. M. Pugh or Dr. S. Narayanswamy

_____ 2022 _____
Dr. M. Debbabi

Abstract

Fatigue Crack Growth Life Assessment Using 3D Finite Element Analysis

Paulian Catalin Ilie

Damage tolerance and fatigue crack growth life assessments allow manufactures to predict the in-service behaviour of high-risk components. Fatigue crack growth solutions are mostly generated using reduced order models that are based on simple geometries (i.e., corner crack at a bolt hole or surface crack in a plate) with the assumption that cracks hold an elliptical shape during propagation. A new finite element-based modelling process that takes into account component geometry, service loading conditions and minimizes simplifications with respect to crack front shape or planarity of the crack growth path is demonstrated.

A 3D finite element-based approach to fatigue crack growth propagation was evaluated as an alternative to reduced order modeling. The modelling approach was verified and validated in three main stages: simple plate geometry, specimens with multiple out of plane cracks, and full-sized specimen panel. A MATLAB analytical solution-based model was developed to estimate crack front evolution and fatigue crack growth life for surface, corner and internal cracks. The analytical results are verified with 3D finite element (FE) based approach implemented in SimModeler Crack. A set of experimental fatigue crack growth measurements based on Al 2024-T3 specimens containing multiple cracks was used to validate the 3D FE modelling solutions. Lastly, fatigue crack growth measurements from a full-sized spar experiment were used to ascertain the accuracy of the proposed FE model.

Acknowledgements

I would like to express my sincere gratitude to my supervisor, Dr. Ayhan Ince, for his continued support over the years, imparting his knowledge, expertise and sparking a passion for the field of Fatigue and Fracture Mechanics in a History student that got lost in the Mechanical Engineering Department.

I would like to thank Dr. Adrian Loghin, for graciously sharing his technical experience, which I hope one day to be worthy of. A debt of gratitude is owed to Dr. Rachel Elliott for sharing her research results and technical expertise.

Thank you to my partner, Elodie, and my parents, without whose love, sacrifices and moral support none of this would have been possible.

Table of Contents

List of Figures

List of Tables

Nomenclature

FEA: finite element analysis

FEM: finite element modeling

FE: finite element

FM: fracture mechanics

SIF: stress intensity factor

CAD: computer aided design

DTA: damage tolerance analysis

DADTA: durability and damage tolerance assessments

ASIP: aircraft structural integrity program

NDI: non-destructive inspection

LEFM: linear elastic fracture mechanics

EPFM: elastic plastic fracture mechanics

$\mathbf{K_I}$ $\mathbf{K_{II}}$ $\mathbf{K_{III}}$**:** mode I, mode II, mode III stress intensity factors

$\boldsymbol{\delta W}$**:** work required to create new surfaces

$\boldsymbol{\gamma}$**:** energy required to form the new surfaces

$\boldsymbol{\delta A}$**:** specific crack growth increment

S: nominal or remote stress

a: crack length

$\boldsymbol{\Delta a_i}$**:** crack incrementation size in the "a" direction

$\boldsymbol{\Delta c_i}$**:** crack incrementation size in the "c" direction

$\boldsymbol{\Delta N_i}$**:** number of cycles associated with the crack increment

Y: geometry factor

E: elastic modulus

R: stress ratio

$\boldsymbol{\gamma_s}$**:** surface energy

$\boldsymbol{\gamma_p}$**:** plastic work

$\boldsymbol{f_{ij}(\theta)}$**:** function of the angle θ

$\boldsymbol{r}$**:** distance between point of interest and crack tip

$\boldsymbol{G}$**:** crack extension force

$\sqrt{EG}$: stress intensity factor

Y: geometry factor

u_i: displacement in the x direction at a node "i"

v_i: displacement in the y direction at a node "i"

θ_0: maximum tangential stress criterion

$\frac{da}{dN}$: fatigue crack growth rate

C: Paris equation coefficient

m: Paris equation exponent

γ: material sensitivity to variations in stress ratio and its influence on crack growth rate.

C_0: axis intercept for R= 0.

K_{max}: maximum stress intensity factor experience by the component

K_c: critical stress intensity factor

K_{eff}: effective stress intensity factor

f: Newman crack closure function

ΔK_{th}: threshold stress intensity range

ΔK: stress intensity range

E: total energy

Π: potential energy of an elastic body

W_s: necessary work for the creation of new surfaces

1 Introduction

1.1 History of Structural Analysis Philosophies

The complexity of man-made structures has gradually increased in step with human understanding of engineering concepts. The phenomenon of metal fatigue has been known since the early 19th century [1] [2]. Technological progress in the transportation, aerospace and defense sectors made over the last 200 years has further accentuated the need to accurately predict fatigue and fracture behaviour in order to prevent catastrophic equipment failures. According to Anderson [3], most structural failures can be attributed to one the following categories: negligence during design, construction or operation; implementation of new design or material elements, which results in an unexpected behaviour. The first category revolves around human nature with the associated shortcomings, errors, ignorance or otherwise wilful neglect. The safety and quality standards that are in place to prevent catastrophic failures are ignored leading to substandard workmanship. The second category involves the adoption of novel techniques which offer significant advantages over traditional methods while containing a non negligible factor of uncertainty. The uncertainty element is managed by extensive analysis coupled testing programs which mitigates risks; however, it does not fully eliminate them [3].

The early days of aeronautical development were marked by a rapid pace of innovation in all aspects of aircraft performance [4]. Advances in structural design and engine performance, as well as, economic obsolescence were often the main drivers for operators deciding to recapitalize fleets. The short lives of fleets prior to the Second World War and the materials from which airplanes were constructed (wood, fabric, copper dominated aluminum alloys) made it such that fatigue life was not a life-limiting issue [4]. In the post war years, aircraft structural integrity policy evolved at a rapid pace, spurred by a series of failures in the commercial and military sectors. The de Haviland DH. 106 Comet was granted its certificate of airworthiness in late January 1952, six months ahead of schedule [5]. By 1954, the aircraft type had suffered several crashes culminating with the grounding of the entire fleet and a halt in production pending the results of a third investigative committee. The inquiries attributed the first two crashes to pilot error and unfamiliarity of the pilots with the new aircraft type [6]. It was also concluded that the crash of

Comet G-ALYP and Comet G-ALYY, in January and April of 1954 respectively, were caused by "sudden cabin failure due to fatigue crack growth followed by the break-up of the aircraft [6].

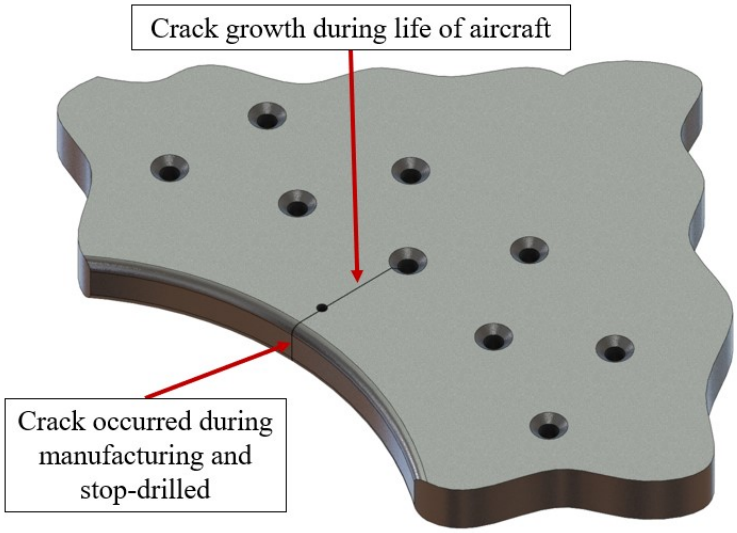

Figure 1 – Possible Failure Origin for Comet G-ALYP [7]
(Reinforcing Plate at Starboard Rear Corner of Front ADF Aerial Window)

Based on the findings of the investigations, "Fail safe" design philosophy was adopted by the aerospace industry which meant that critical structural components had to achieve their design fatigue life and any damage sustained had to be detectable before a loss of safety [8].

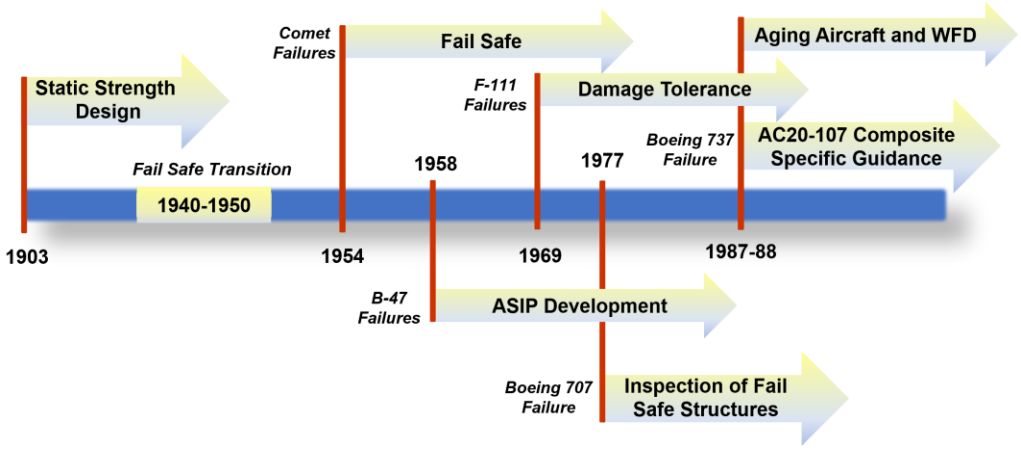

Figure 2 – Evolution of Aircraft Structural Integrity Philosophies [8].

The end of the Second World War saw the rapid development of the next generation of strategic bombers. The B-47 entered production in late 1948 and continued until 1957, during

which time a total of 2041 aircraft were made by three different manufacturers (Boeing, Douglas and Lockheed) [9]. The aircraft type was accepted into service based on a combination of static tests supplemented by subsequent flight load surveys focused on high loads [9]. Ground based tests demonstrated that the aircraft could sustain at least 150% of its design load limit, however, no fatigue/cyclic load testing was conducted and no expected life was predicted. The airplane was expected to be in service at least until 1965 when the next generation of strategic bombers could replace it. The lack of thorough validation during the preliminary stages of production culminated in March and April 1958 when five bombers were lost, three of which accumulated less than 1500 flight hours. These crashes, attributed to metal fatigue, resulted in an emergency inspection program which later became an integral part of the Air Force's approach to designing, manufacturing and operating its fleet of high-performance aircraft.

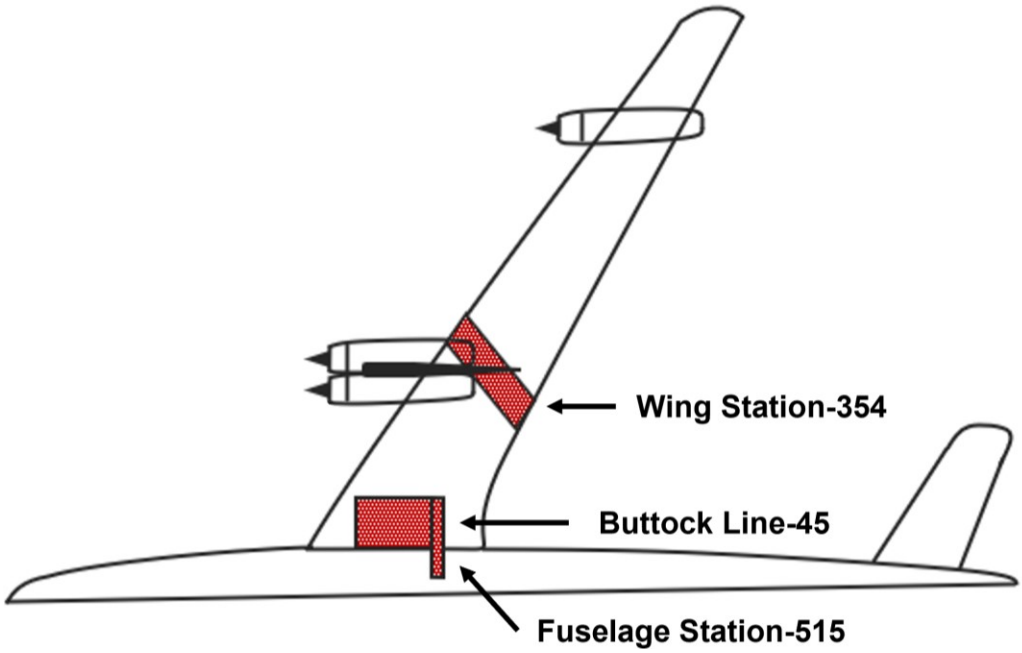

Figure 3 – Diagram of Critical Fatigue Locations of the B-47 Aircraft [7].

The Aircraft Structural Integrity Program (ASIP) was implemented to solve the fatigue issues plaguing the B-47's wings and longerons. In the following months the program was adopted by all major commands with the stated goals: "(a) to control structural fatigue in the operational aircraft fleet, (b) to devise methods of accurately predicting aircraft service life, and (c) to provide the design know-how and test techniques required to avoid structural and sonic fatigue problems in future weapons systems" [9].

The program continued to evolve over the years to capture changes and innovations related to the original outlined concepts from 1959, as such, the fundamental objectives stated in ASIP documentation remained unchanged until 1969. The F-111 was designed according to ASD TR 66-57 (Air Force Structural Integrity Program: Airplane Requirements) which required a combination of full-scale fatigue tests and standard stress-life fatigue analysis on the basis of Miner's rule. The regulations did not account for the presence of flaws in components and put a strong emphasis on the use of single load path structures [7]. The crash of an F-111A due to a wing pivot fitting fracture resulted in the implementation and adoption of durability and damage tolerance assessments (DADTA). The failure of the wing pivot (Figure 4) happened after only 107 airframe flight hours, during a 3.5g maneuver, well within the design limit load factor of the airframe [8]. The cause of the crash was traced to a manufacturing defect during forging that acted as an initiation site in a low toughness material [7].

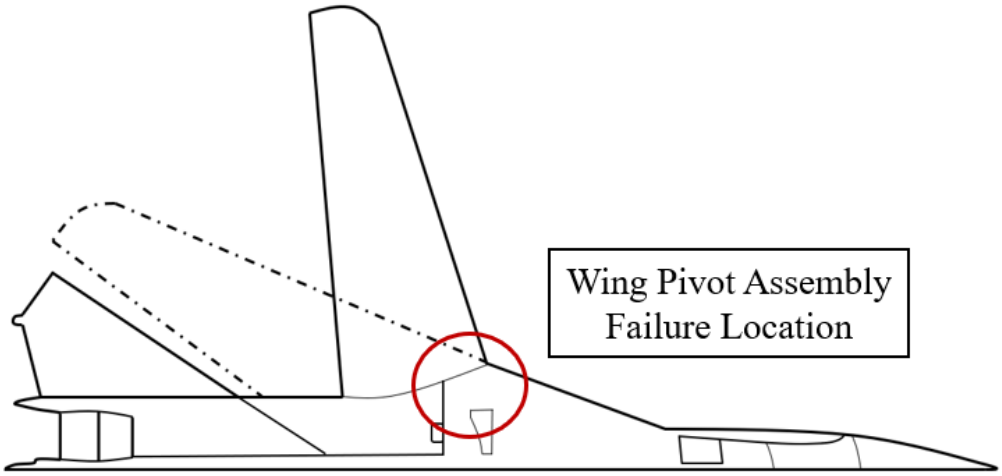

Figure 4 – F-111 Wing Pivot Fitting Failure Location.

The two-phase recovery program employed a cold proof test campaign to determine the probable size of flaws present in single load path elements and an improved NDI reinspection program based on the principles of damage tolerance analysis (DTA). A subsequent revision of ASIP documentation was recorded in MIL SPEC 83444 (1974) and MIL STD-1530A (1975) which differed from the fail-safe philosophy of the 1950s in the following respects [8]:

- The presence of small or undetectable flaws in components had to be assumed and taken into consideration as part of the certification process.
- Components can be inspectable or non inspectable in service:

- ❖ Components considered inspectable, need to be certified as Fail-Safe or slow crack growth structure, by demonstrating crack initiation and growth can be safely detected between inspection intervals.
- ❖ Components considered non-inspectable, need to demonstrate safe operations for two design service lives (as calculated with fatigue crack growth methodologies) with the presence of an initial flaw.

Modern implementations of ASIP principles, both in the military and civilian aerospace sectors, have reduced hull losses by approximately 80% [10]. Accidents, such as, the Dan Air Boeing 707 (1978) and the Aloha Airlines Boeing 737 (1988) created amendments (inspections of fail-safe structures) or new regulations (widespread fatigue damage and associated service life limits) to the existing standards for structural integrity. Ensuring that complex aeronautical systems are airworthy throughout their expected operational life is an evolutionary process that necessitates structures to withstand predicted load spectra in the presence of manufacturing defects, fatigue and environmental factors until such a time that the damage is visible and detectable at regular inspection intervals.

1.2 Fatigue Crack Growth

The modern incarnation of fracture mechanics has its roots in the work performed by Alan A. Griffith, published in 1920. By analyzing unstable crack propagation in elliptical holes, the presence of a quantitative link between flaw size and fracture stress was demonstrated [3]. The model accurately predicted crack behaviour in brittle materials. The energy release rate concept, established by George R. Irwin in 1956, was an extension of Griffith's theory that could be applied to ductile materials. Irwin's [11], [12] energy release rate concept linked displacement near the crack-tip and stresses through a constant, later termed as the stress-intensity factor. Griffith [13] proposed that the work required to create new surfaces (δW) during crack propagation is equal to the energy required to form the new surfaces (γ) for that specific crack growth increment (δA):

$$\delta W = \gamma \delta A \tag{1}$$

He demonstrated that the breaking load equation for an infinitely wide plate containing a crack and under remote tensile stress was [14]:

$$S_c = \left(\frac{2E\gamma_s}{\pi a}\right)^{1/2} - plane\ stress \tag{2}$$

$$S_c = \left(\frac{2E\gamma_s}{\pi a(1-v^2)}\right)^{1/2} - plane\ strain \tag{3}$$

$$G \geq G_c = \frac{S_c^2 \pi a}{E} = 2\gamma_s - plane\ stress \tag{4}$$

$$G \geq G_c = \frac{S_c^2 \pi a}{E}(1-v^2) = 2\gamma_s - plane\ strain \tag{5}$$

G – strain energy release rate

S_c – macro stress (nominal or reference) necessary for fracture

By considering the energy changes in the plate as a whole, it was possible to avoid the highly strained region near the crack tips and derive a representative expression of the macro-stress. Irwin further developed this approach by modifying the specific surface energy parameter γ to include the work caused by plastic deformation in small regions ahead of the crack edge.

$$\gamma_{eff} = \gamma + \gamma_p \tag{6}$$

In 1957, Irwin [12] concluded that the stress field near the crack tip (in plane strain or plane stress conditions) could be generalized in terms of two parameters: a uniform stress parallel to the direction of crack extension and -*at the time novel parameter*- the stress intensity factor. It was demonstrated that near the crack tip the main part of any component of the stress tensor was [12], [14]:

$$\sigma_{ij} = \sqrt{EG}\,\frac{1}{\sqrt{2\pi r}} f_{ij}(\theta) \tag{7}$$

$f_{ij}(\theta)$ – function of the angle θ

r – distance between point of interest and crack tip

G – crack extension force

$\sqrt{EG}$ – stress intensity factor

By demonstrating the relationship between the strain energy release rate and the stress intensity factor, Irwin showed that the energy method as first envisioned by Griffith was analogous to the strength approach in the context of linear elastic fracture analysis [13].

$$G_I = \frac{\left(S\sqrt{\pi a}Y\right)^2}{E} = \frac{K_I^2}{E} - plane\ stress \tag{8}$$

$$G_I = \frac{\left(S\sqrt{\pi a}Y\right)^2}{E}(1-v^2) = \frac{K_I^2}{E}(1-v^2) - plane\ strain \tag{9}$$

In 1955, Paul C. Paris, then a faculty associate at the Boeing Company was sent to England to examine the de Havilland Comet crashes as part of an ongoing effort to develop the first American commercial jet [15]. The application of fracture mechanics to fatigue crack propagation, as envisioned by Paris et al. [16], was eventually published after several years of editorial opposition in spite of compelling theoretical and experimental arguments.

Stress intensity factor (SIF) or stress field parameter is a fundamental element in fracture mechanics, it is defined as:

$$K_I = S\sqrt{\pi a}Y \tag{10}$$

where:

S – nominal or remote stress

a – crack length

Y – geometry factor

It is able to predict the magnitude of stresses, strains and displacements at the crack tip region by combining nominal stress, crack geometry, loading conditions and cracked body geometry. In the above equation, the geometry factor Y, includes the effects of crack and body shape as well as the type of loads and boundary conditions. The value of Y is generally derived using uniform remote or nominal stress, S. In cases of non-uniform stress distributions, the maximum stress is used to calculate the stress field parameter.

Within the context of fracture mechanics there are methods able to characterize experimental fatigue crack growth data such as the Paris equation [16], Walker equation [3], Forman equation [3], NASGRO [17] and AFGROW [18]. These equations are able to capture specific regions or the entire crack growth behaviour from the threshold point to fracture toughness, as well as,

account for variations in R ratio. Based on experimental observations, crack growth is divided into three main regions:

- Region I – threshold
- Region II – stable crack growth
- Region III – unstable crack growth

Equations (11), (12), (13), (14), (15) were introduced to predict FCG behaviour shown in Figure 5, specifically how crack growth rate changes as a function of the stress intensity factor. The Paris-Erdogan equation focuses on region II (Figure 5) and it does not consider R ratio. Paris and Erdogan were able to identify empirically the relationship between ΔK and crack growth rate. Experimental data showed the crack growth behaviour within region II can be approximated as linear, thus, in a log-log graph m is the slope of the line.

$$\frac{da}{dN} = C(\Delta K)^m \tag{11}$$

The Walker model [3] modified the Paris-Erdogan approach in order to account for the mean stress effect on fatigue crack growth rate throughout the stable crack growth region (Region II).

$$\frac{da}{dN} = C_0 \left(\frac{1}{(1-R)^{1-\gamma}} \Delta K\right)^m \tag{12}$$

γ – material sensitivity to variations in stress ratio and its influence on crack growth rate.
C_0 – axis intercept for R= 0.
Forman [3] proposed an equation that described Region II and Region III:

$$\frac{da}{dN} = \frac{C\Delta K^m}{(1-R)K_c - \Delta K} = \frac{C\Delta K^{m-1}}{\frac{K_c}{K_{\max}} - 1} \tag{13}$$

As K_{max} approaches the material toughness value, the crack growth rate tends towards infinity. This model was further developed by Forman, Newman, de Koning and Henriksen [19], [20] as part of their research at NASA, NLR and ESA:

$$\frac{da}{dN} = C(\Delta K)^m \frac{\left(1 - \frac{\Delta K_{th}}{\Delta K}\right)^p}{\left(1 - \frac{K_{max}}{K_c}\right)^q} - \text{Simplified} \quad (14)$$

$$\frac{da}{dN} = C_0 \left[\left(\frac{1-f}{1-R}\right)\Delta K\right]^m \frac{\left(1 - \frac{\Delta K_{th}}{\Delta K}\right)^p}{\left(1 - \frac{K_{max}}{K_c}\right)^q} - \text{Complete} \quad (15)$$

f – Newman crack closure function

C_0 – axis intercept constant for a stress ratio of 0

ΔK_{th} - threshold stress intensity range

ΔK – stress intensity range

K_{max} – maximum stress intensity value

K_c – fracture toughness/critical stress intensity

The complete form of the equation is able to describe crack growth behavior in all three regions of Figure 5. Furthermore, it accounts for crack closure and R ratio throughout the entire crack growth regime.

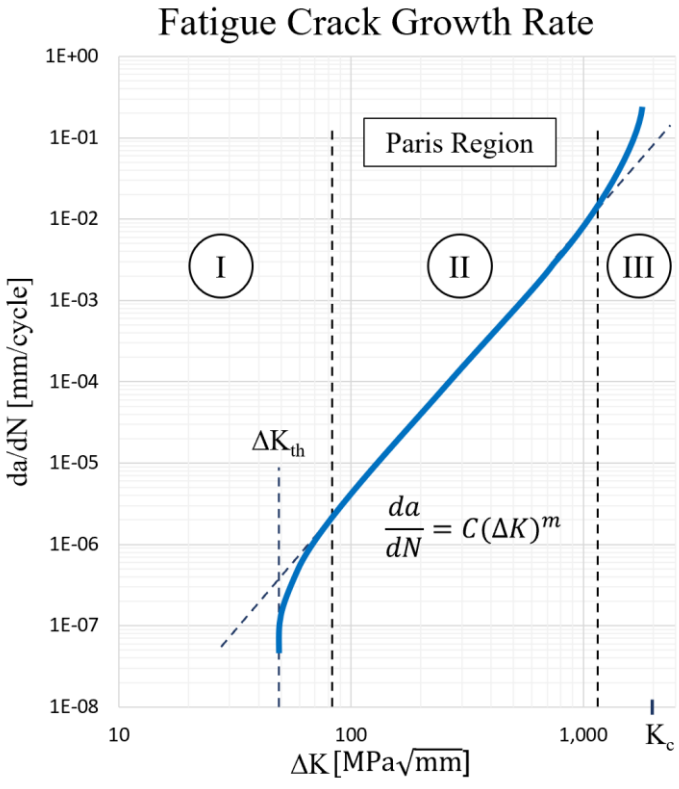

Figure 5 – Typical fatigue crack growth curve.

Experimental observations of crack behaviour determined the process takes place in three distinct phases [3]:

- A free surface is created near an inclusion, grain or second phase particle by cracking of the particle or interface decohesion.
- Remote loading stresses acting on the hollow region further increase its size.
- Void growth interacts with nearby voids resulting in coalescence.

The underpinning principles of LEFM, developed by Griffith and later modified by Irwin, state that a crack will propagate when the stress intensity value near the crack tip is greater than the fracture toughness of the material. The Griffith approach necessitates an increase in surface energy from the creation of two new free surfaces, such that, the loss of potential energy is less or equal to increase in surface energy as the crack propagates [21].

$$\frac{dE}{dA} = \frac{d\Pi}{dA} + \frac{dW_s}{dA} \tag{16}$$

$$-\frac{d\Pi}{da} \geq \frac{dW_s}{da} \tag{17}$$

Solving for the fracture stress for a through crack inside an infinitely wide plate under tensions gives the following equation:

$$\sigma_f = \left(\frac{2E\gamma_s}{\pi a}\right)^{1/2} \tag{18}$$

Applied to brittle solids, γ_s represents the total energy of broken bonds (surface energy) which allows for crack formation and growth. Irwin modified the approach outlined above to include materials capable of plastic flow by adding γ_p, which is defined as plastic work per unit of created surface area:

$$\sigma_f = \left(\frac{2E\left(\gamma_s + \gamma_p\right)}{\pi a}\right)^{1/2} \tag{19}$$

The application of LEFM approach to fatigue analysis requires the size of the plastic zone to be small compared to crack size and part geometry and the assumption that material behaviour can be approximated as linear-elastic.

Once a crack has initiated, it can be classified into any of the three main categories or a combination thereof [3]:

- Mode I: Crack faces are opened by a load applied normal to the crack plane.
- Mode II: In-plane shear stresses, acting normal to the leading edge, force the crack faces to slide.
- Mode III: Forces acting parallel to the leading-edge result in a tearing action.

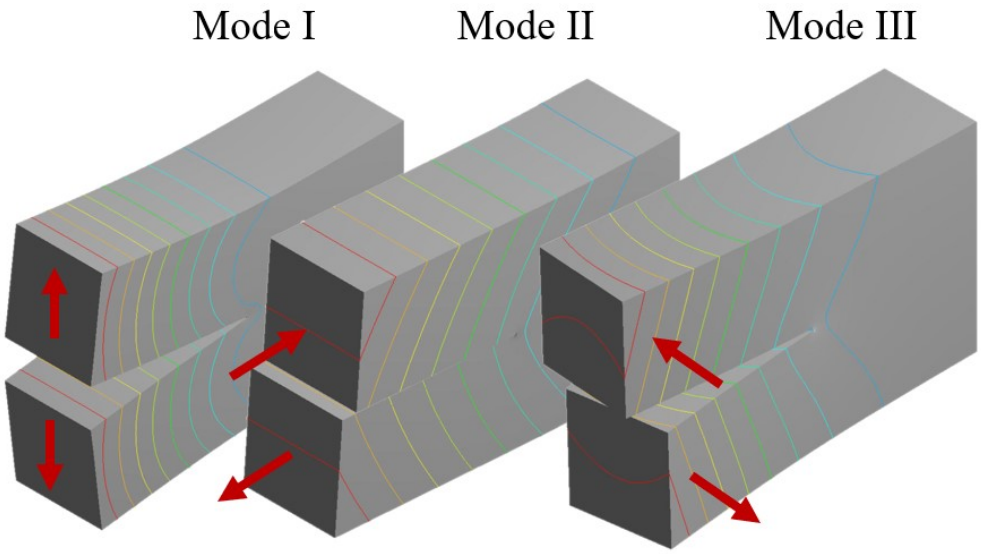

Figure 6 – Crack Loading Modes

Geometric features, discontinuities, inclusions and manufacturing defects increase local distribution of stresses which can lead to crack initiation and subsequent propagation. Stress intensity factors (SIF) quantify the stress singularity found at the crack tip, these values can be expressed as K_I (Mode I opening), K_{II} (Mode II in-plane shear), K_{III} (Mode III out of plane shear).

Early approaches to characterizing material behaviour put emphasis on materials' static properties such as yield stress, ductility, fatigue and creep. The classic approach proved inadequate in accurately predicating material behaviour of aeronautical components. The adoption of fracture mechanics presented a new set of challenges, one that requires an in-depth understanding of crack initiation, propagation and effect of ductility or brittleness on crack growth. The amount of plastic deformation that a part undergoes before fracture will determine if the fracture is brittle or ductile.

The ability to resist a brittle fracture as the crack grows through the material is called fracture toughness K_{IC} [22]. Figure 7 shows the relation between remote stresses (σ) and fracture toughness. LEFM is applied in conditions where fracture toughness is relatively low and plastic deformation is confined to very small regions by remaining below 0.8 σ_y. For loading conditions above 0.8 σ_y, remote stress and K_{IC} no longer vary linearly which requires elastic-plastic fracture mechanics (EPFM) to predict material behaviour. In case of high fracture toughness, fracture mechanics is no longer applicable due to failure stress' insensitivity to toughness, as such, a limit load analysis can be used to calculate failure stresses [3].

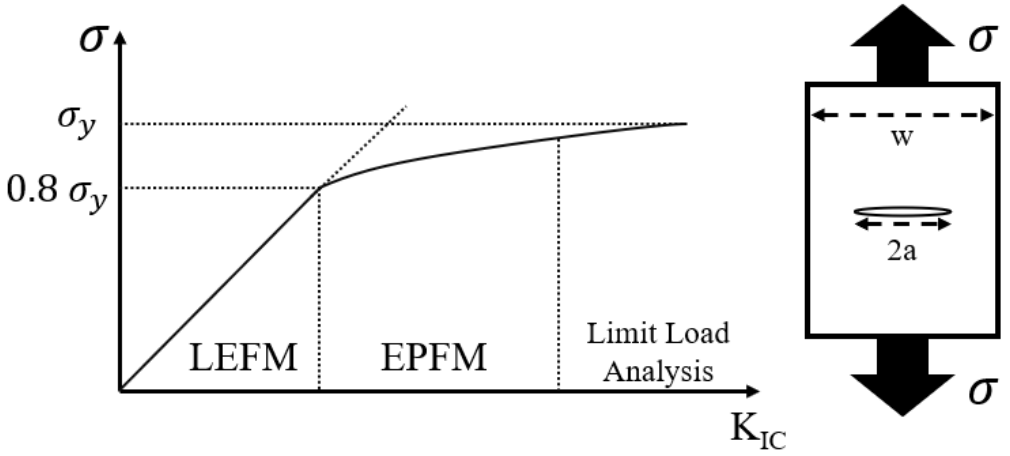

Figure 7 – Variation of remote stress and fracture toughness.

Figure 8 shows the plastic region where localized yielding is taking place and the surrounding stress intensity field.

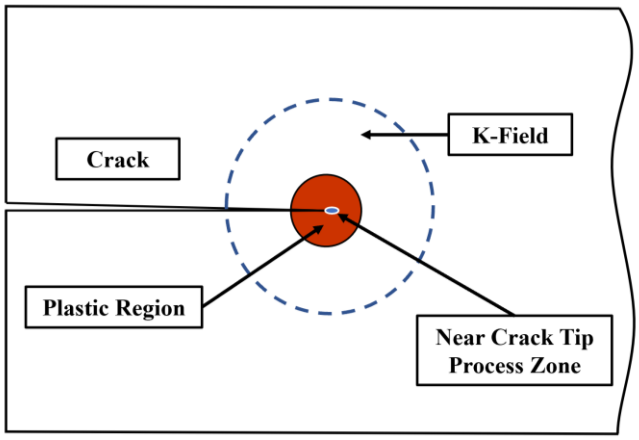

Figure 8 – Plastic Region and stress intensity field surrounding crack tip.

In addition to fracture toughness, stress intensity field and localized plastic deformation, Poisson effects can influence the results of an LEFM approach. In isotropic and orthotropic materials, a plane stress condition occurs when there are no out of plane shear strains and no out-plane normal stresses, meaning all stresses act in the same plane. Plain strain condition applies when there are no strains acting in the direction normal to the axis of the remote tensile stress as well as the direction of the crack propagation. Components with small transverse thickness are generally considered in a state of plane stress, for components with thick transverse dimensions, the crack tip is considered to be under plane strain.

1.3 Crack Growth Analysis

1.3.1. Numerical Procedure

Damage tolerance assessments use fracture mechanics principles to quantify the impact of imperfections on the life of structural components in their expected operating environment. The stress intensity factor as outlined above serves the essential role of relating the energy release rate at the crack tip to the fatigue crack growth rate [Paris-Erdogan]. Crack propagation can be modeled using closed form solutions of mode I stress intensity factors (K_I) for simple component/crack geometries while for complex load configurations and geometries the weight function technique [23], [24] or finite element analysis (FEA) can be employed. There are several FEA solutions to calculating stress intensity factors, such as the stiffness derivative technique [25], the *J*-integral [26], inverse square root singularity of stresses [27] and a variety of methods using near-tip displacements [28]. The FEA approach can generate stress, strains, displacement and strain energy in the context of numerically based fatigue crack growth analysis. These quantities are then used to determine stress intensity factors, fatigue life and crack growth direction. Adaptive remeshing techniques used to determine crack growth behaviour have the ability to solve problems containing complex geometries defined by intricate boundary and loading conditions. Figure 9 shows the four main steps of that make up the adaptive remeshing technique [29]:

- Creation of a 3D FE model
- Computation of K_{eff} along the crack front
- Incrementation of the crack front according to applicable fatigue crack growth laws
- Creation of a new 3D FE model containing the incremented crack front.

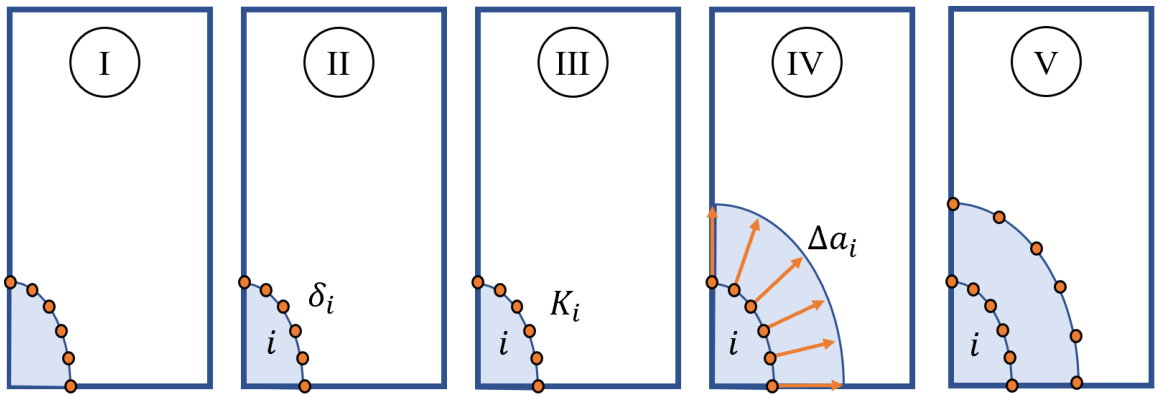

Figure 9 – Adaptive remeshing technique [29].

Generally, crack fronts are defined according to either a two-degree-of-freedom or multiple-degree-of-freedom model. The first model is based on a pre-defined crack geometry with variable aspect ratio, and analyzes crack growth at two points along the crack edge [29]. The overall crack shape is maintained throughout its entire length, as such, the approach is not suitable for large deviations in crack geometries, out-of-plane crack growth or complex loading conditions. The second model, divides the crack front in multiple elements and creates the geometry through polygonal lines or cubic splines. The higher degree of refinement along the crack front is associated with more precise geometry, SIF results, and versatility (i.e., planar or out-of-plane crack propagation, complex boundary and loading conditions) [29]. A numerically based alternative to the methods described above was proposed by Belytschko [30], able to solve crack growth problems with minimal remeshing. The extended finite element method (XFEM) reduces the remeshing requirements associated with classic FEA techniques by using a displacement field approximation to define arbitrary discontinuities and near-tip asymptotic crack fields, which in turn necessitate minimal mesh refinement [31]. Moes et al [31] demonstrated that 3D crack geometries could be propagated using the X-FEM method and the computed stress intensity factors, essential for crack orientation and magnitude of the crack front velocity, were in good agreement with analytic and benchmark solutions.

1.3.2. Analytical

In practical applications, Newman and Raju's [32] empirical SIF solutions can be applied to numerous crack configurations under remote uniform bending or tensile loads and require less time to solve than 3D FEA based sequential crack propagation simulation. Analytical approaches

generally tend to arrive at conservative results, however, in some cases where the reduced order model is not representative of the specific component failure location the closed form solutions may be non conservative [33].

Irwin [34] was able to define stress and displacement fields around a crack front in a linear elastic solid by relating the strain energy release rate to the stress intensity factor. Stress intensity factor solutions for finite bodies containing embedded elliptical, corner and surface cracks require approximate analytical methods [32]. Various analytical methods for finite geometries have been proposed such as: Smith et al [35] (crack front SIF values calculated with the alternating method), Raju and Newman [36] (finite element method), Heliot et al [37] (boundary-integral equation method), Fawaz and Anderson (p-version FE method) [38], Bombardier and Liao (compounding superposition method) [39],

1.4 Outline

Validation and verification of the 3D FEA approach was separated in three distinct stages: 3D single flaw cracked plate with 3 different crack geometries (verification), multiple flaw plate with out-of-plane crack propagation (validation), complex large scale spar structure (validation). The fatigue crack growth modelling approach was assessed with three different crack configurations. A rectangular plate model was selected for the verification stage. Three types of cracks (semi-elliptical, embedded elliptical and quarter elliptical cracks) were evaluated individually by inserting them at the center of the model. A uniform tensile loading was applied to all crack configurations. An analytical model implemented in MATLAB was used to generate fatigue life, crack growth and crack path values. The three sets of analytical results (semi-elliptical, embedded elliptical and quarter elliptical cracks) were generated using closed form SIF equations as published by Newman and Raju [32], [40]. A CAD model using the same geometry and material properties was imported in the SimModeler 3D FEA software package. FCG simulations were run for the three types of cracks under investigation. The generated results were in good agreement, thus, verifying the 3D FEA method against the analytical model.

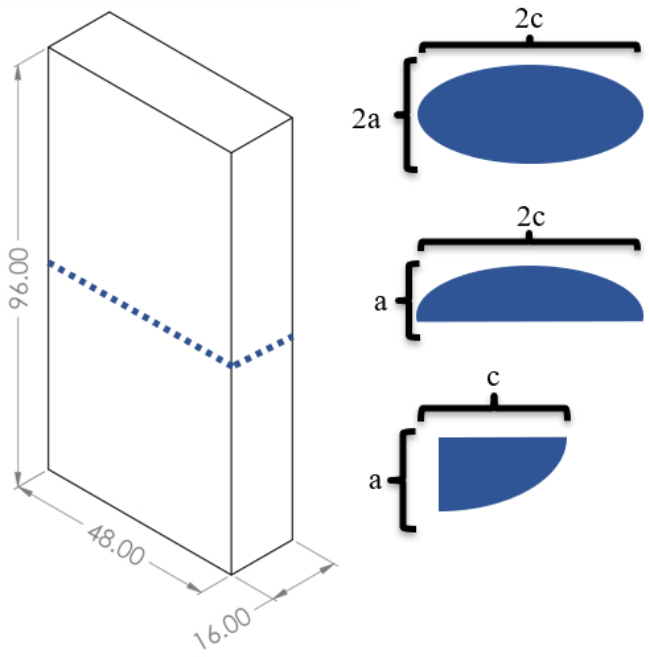

Figure 10 – Simple plate model geometry and crack configurations.

The SimModeler Crack FEA approach was validated with experimental results from two specimen configurations containing multiple out of plane cracks. An aluminium plate CAD model was created based on the work of Kim et al. [41] with two different crack configurations being simulated. Five through cracks were initiated from notches at different locations around rivet holes. The specimens were subjected to tensile loading conditions. Experimental crack path and crack length measurements were compared with the 3D FEA results. Compared results show that the FEA provided accurate predictions.

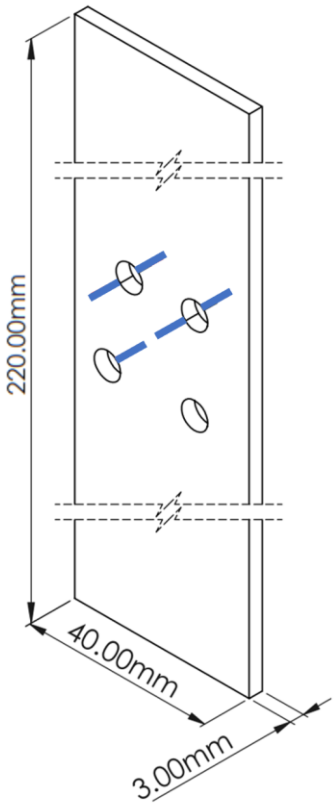

Figure 11 – Multiple flaw specimen geometry and crack configuration.

Experimental Procedure

In stage three, experimental measurements of full-sized component test [42] are used as a reference for modeling validation purposes. A complete wing spar was tested in tension to characterize fatigue crack growth behaviour at three locations. Crack 1 was initiated from a notch at a rivet hole as shown in Figure 12. The crack propagated under far field cyclic tensile loading until fracture was reached through the bottom of the web. Crack 2 was initiated and propagated under tensile loading conditions until fracture. Crack 3 was initiated at the rivet hole and grown under tension through the width of the spar's web.

Modeling Procedure

A simplified CAD model was created. It contained two rows of five rivet holes and two spar caps (upper and lower) attached to the web. A crack geometry representative of the initiated crack was inserted and propagated with the aid of a 3D FEA software (SimModeler Crack). All three cracks were simulated individually and solution for loading cycles, crack length and crack path were

generated. Experimental measurements and numerical solutions are presented and analyzed in section 3.

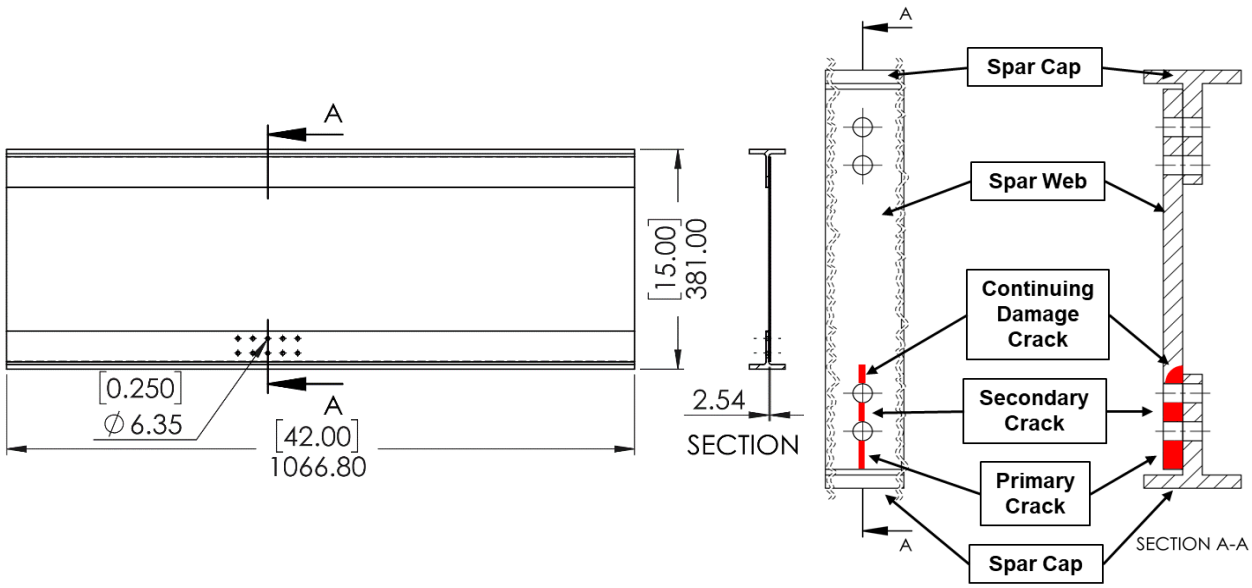

Figure 12 – Spar Geometry and crack locations.

1.5 Scope of the research

Computer aided simulation techniques have been extensively applied to the field of fatigue crack growth. The adapted 3D FEA modelling technique can be applied to complex geometric models to predict fatigue crack growth behaviour. The scope of this research is to demonstrate the accuracy of the proposed FEA approach through validation and verification.

The objectives of this work can be outlined as such:

- Simple geometry level verification: Implement three different configurations of single planar cracks in an analytical model and a model using the FEA technique. Analyze and compare the results.
- Specimen level validation: Modeling validation is reached using two experimental measurements.
- Full sized component validation: Simulate fatigue crack growth in a full-sized wing spar. Generate results for three different cracks, perform deterministic analysis to account for material properties variation and test setup misalignments. Compare numerical solutions against experimental data.

2 Analytical Modeling and Methodology

The analytical modeling approach, used as part of this research, was defined as a complete crack growth calculation process that employed stress intensity factors derived from 3D FEA which cover numerous configurations parameters [32]. Results for stress intensity factor (K_I) can be generated numerically as part of 3D FEA solvers for realistic component geometry and loading conditions or analytically using reduced order models for simplified geometries and loading conditions. The analytical solutions presented in this section use only mode I crack propagation within the Paris region of the fatigue crack growth regime (Figure 5) for two-dimensional cracks. Figure 13 describes the analytical methodology employed to calculate crack growth life:

i. Initial load and crack conditions (applied remote stress, crack length and geometry factor) are used to determine the stress intensity factor range (ΔK).

ii. The Paris equation is numerically integrated to calculate increments of crack length for a given number of cycles (ΔN) at R=0 (where $R=\sigma_{min}/\sigma_{max}$).

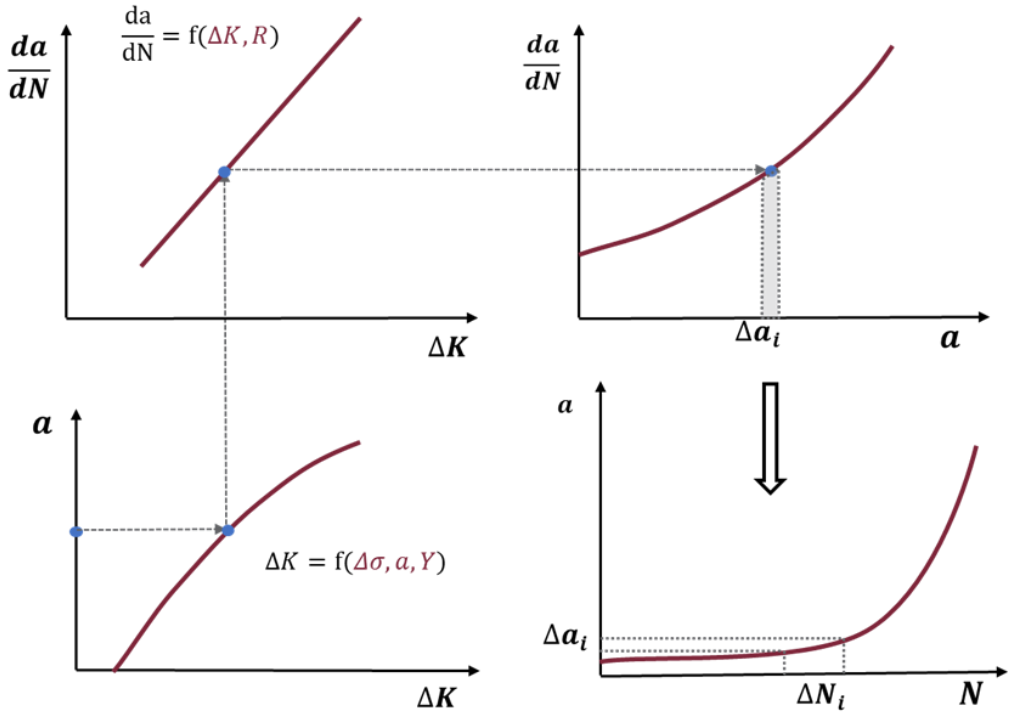

Figure 13 – Numerical integration technique applied to fatigue crack growth.

Initial crack geometry is defined with two vertices (a_0, c_0). The i^{th} increment in the semi-minor and semi-major directions are Δa_i and Δc_i for all elliptical crack configurations used in this

research. The aspect ratio of the crack model varies throughout the propagation process based on the generated crack increments. The numerical integration technique, shown in Figure 14, is used to calculate the SIF as a function of stress, crack length and geometry factor. The crack growth rate is calculated based on the SIF value and the stress ratio which is then used to determine the crack incrementation size (Δa_i). The number of cycles associated with the crack increment (ΔN_i) is calculated in the last step. The overall crack geometry is updated and the process is repeated until fracture or a stop condition is reached.

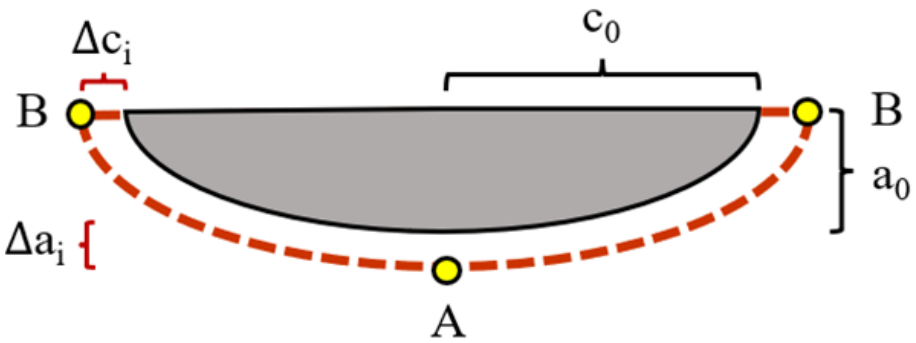

Figure 14 –. Typical surface semielliptical crack geometry.

The analytical modeling approach employs two vertices that define crack front edge in an elliptical, semi elliptical or a quarter-elliptical crack shape (Figure 14). Overall crack shape as the crack propagates through the model was determined based on the numerical solution of Eqs. (20)-(23) on the basis of the stress intensity factors at two crack frontal locations of A and B (i.e. ΔK^A, ΔK^B)

$$\frac{\Delta a_i}{\Delta N_i} = C(\Delta K_i^A)^m = C(\Delta S_i\sqrt{\pi a_{i-1}}Y_{i-1}^A)^m; \tag{20}$$

$$a_i = a_o + \sum_{i=1}^{N} \Delta a_i \,; \Delta a_i = C(\Delta S_i\sqrt{\pi a_{i-1}}Y_i^A)^m \Delta N_i \tag{21}$$

$$\frac{\Delta c_i}{\Delta N_i} = C(\Delta K_i^B)^m = C(\Delta S_i\sqrt{\pi a_{i-1}}Y_{i-1}^B)^m \tag{22}$$

$$c_i = c_o + \sum_{i=1}^{N} \Delta c_i \,; \Delta c_i = C(\Delta S_i\sqrt{\pi a_{i-1}}Y_i^B)^m \Delta N_i \tag{23}$$

The closed form SIF solutions proposed by Newman and Raju can account for variations in loading conditions (bending or tension), crack depth, crack length and plate thickness [32]. The current research presented herein focused on a single plate geometry containing three different

crack types: surface elliptical, embedded elliptical and corner quarter-elliptical (Figure 15). Analytical SIF solutions based on [32], [40] were implemented using MATLAB scripts to generate analytical FCG solutions for the three aforementioned crack types so as to verify the results generated with the FEA approach. The analytical model replicated uniform tensile loads to the top surface and the bottom surface was fixed to prevent rigid body motion. The model geometry is 96 mm in length, 48 mm in width ($2W$ *or* W) and 16 mm thick (t). The crack geometry in all three configurations is 2 mm (a) and 3 mm (c). The surface semi-elliptical configuration was tested at multiple load levels. The embedded elliptical and surface elliptical was tested at a single load level (200 MPa). Ti-6Al-4V was used for the 2D analytical model (Table 1).

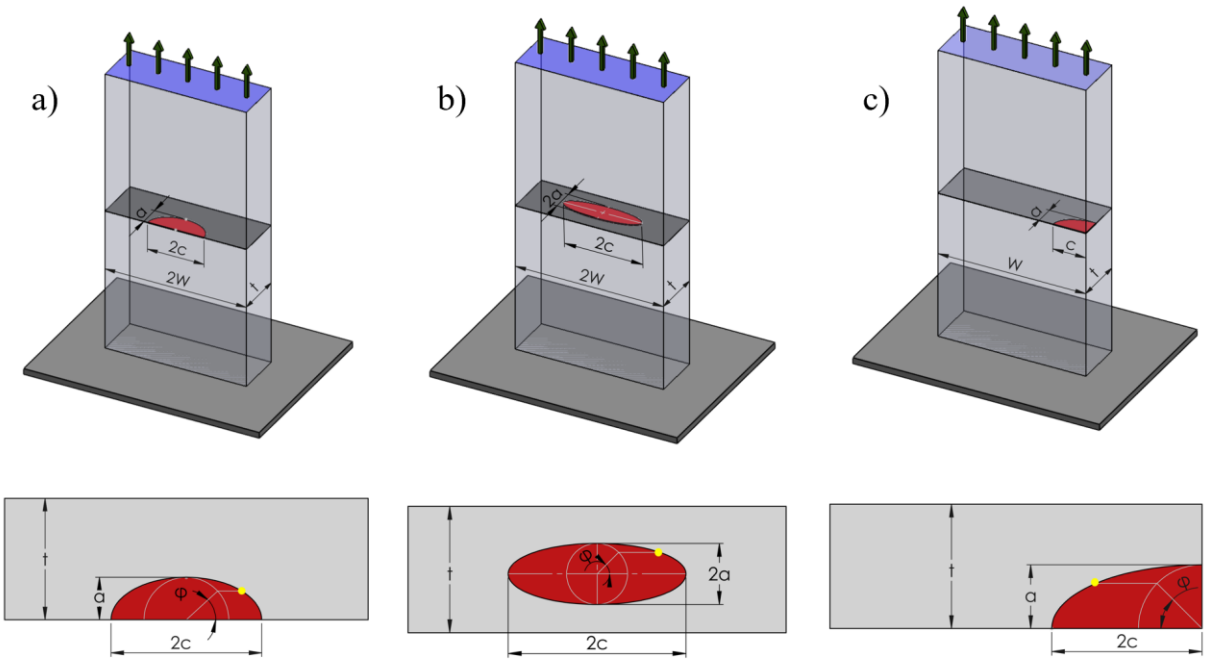

Figure 15 – Surface Elliptical Crack (a), Embedded Elliptical Crack (b), Corner Quarter-Elliptical Crack (c).

Figure 15 shows the three tested configurations and the associated geometry parameters (a, c, W, t, ϕ). These geometry parameters are used in the equations (24) – (54).

SIF solution of the semi-elliptical crack for the analytical model is based on the numerical solutions of equations (24) – (54) [32]:

$$\Delta K_I = (\Delta\sigma)\sqrt{\frac{\pi a}{Q}}F\left(\frac{a}{t}, \frac{a}{c}, \frac{c}{W}, \varphi\right) \tag{24}$$

$$F = \left[M_1 + M_2\left(\frac{a}{t}\right)^2 + M_3\left(\frac{a}{t}\right)^4\right] f_\varphi f_w g \tag{25}$$

$$M_1 = 1.13 - 0.09\left(\frac{a}{c}\right) \tag{26}$$

$$M_2 = -0.54 + \frac{0.89}{0.2 + \frac{a}{c}} \tag{27}$$

$$M_3 = 0.5 - \frac{1.0}{0.65 + \frac{a}{c}} + 14\left(1.0 - \frac{a}{c}\right)^{24} \tag{28}$$

$$f_\varphi = \left[\left(\frac{a}{c}\right)^2 \cos^2\varphi + \sin^2\varphi\right]^{1/4} \tag{29}$$

$$f_w = \left[\sec\left(\frac{\pi c}{2W}\sqrt{\frac{a}{t}}\right)\right]^{1/2} \tag{30}$$

$$g = 1 + \left[0.1 + 0.35\left(\frac{a}{t}\right)^2\right](1 - \sin\varphi)^2 \tag{31}$$

Where:

a: crack length semi-minor axis.

c: crack length semi-major axis.

W: width of the plate.

t: thickness of the plate.

ϕ: angle crack geometry

Embedded elliptical crack SIF equations [32]:

$$\Delta K_I = \Delta\sigma F\sqrt{\frac{\pi a}{Q}} \tag{32}$$

$$F = (M_1 + M_2\lambda^2 + M_3\lambda^4) \cdot g \cdot f_\varphi \cdot f_w \tag{33}$$

$$M_2 = \frac{0.05}{0.11 + \left(\frac{a}{c}\right)^{1.5}} \tag{34}$$

$$M_3 = \frac{0.29}{0.23 + \left(\frac{a}{c}\right)^{1.5}} \tag{35}$$

$$\lambda = \frac{a}{a + d} \tag{36}$$

$$f_w = \left[\sec\left(\frac{\pi c}{2W}\sqrt{\frac{2a}{t}}\right)\right]^{1/2} \tag{37}$$

$$g = 1 - \frac{\lambda^4\sqrt{2.6 - 2\lambda}}{1 + 4\lambda}|\cos\varphi| \tag{38}$$

For a/c ≤1:

$$f_\varphi = \left[\left(\frac{a}{c}\right)^2 \cos^2\varphi + \sin^2\varphi\right]^{1/4} \tag{39}$$

$$M_1 = 1 \tag{40}$$

$$Q = 1 + 1.464\left(\frac{a}{c}\right)^{1.65} \tag{41}$$

For a/c >1:

$$f_\varphi = \left[\left(\frac{c}{a}\right)^2 \sin^2\varphi + \cos^2\varphi\right]^{1/4} \tag{42}$$

$$M_1 = \sqrt{\frac{c}{a}} \tag{43}$$

$$Q = 1 + 1.464\left(\frac{c}{a}\right)^{1.65} \tag{44}$$

Corner (quarter elliptical) crack SIF equations [32]:

$$\Delta K_I = \Delta\sigma F\sqrt{\frac{\pi a}{Q}} \tag{45}$$

$$Q = 1 + 1.464\left(\frac{a}{c}\right)^{1.65} \tag{46}$$

$$F = \left[M_1 + M_2\left(\frac{a}{t}\right)^2 + M_3\left(\frac{a}{t}\right)^4\right] g_1 g_2 f_\varphi f_w \tag{47}$$

$$M_1 = 1.08 - 0.03\left(\frac{a}{c}\right) \tag{48}$$

$$M_2 = -0.44 + \frac{1.06}{0.3 + \frac{a}{c}} \tag{49}$$

$$M_3 = -0.5 - 0.25\left(\frac{a}{c}\right) + 14.8\left(1 - \frac{a}{c}\right)^{15} \tag{50}$$

$$g_1 = 1 + \left[0.08 + 0.4\left(\frac{a}{t}\right)^2\right](1 - \sin\varphi)^3 \tag{51}$$

$$g_2 = 1 + \left[0.08 + 0.15\left(\frac{a}{t}\right)^2\right](1 - \cos\varphi)^3 \tag{52}$$

$$f_\varphi = \left[\left(\frac{a}{c}\right)^2 \cos^2\varphi + \sin^2\varphi\right]^{1/4} \tag{53}$$

$$f_w = \left[\sec\left(\frac{\pi c}{2W}\sqrt{\frac{a}{t}}\right)\right]^{1/2} \tag{54}$$

The crack propagation is achieved in increments of Δa_i (measured along the depth of the plate) and Δc_i (measured along the face of the plate). The operation is performed within the analytical model using an input of applied loading cycles which is then translated into fatigue crack propagation life of a-N results as shown in the above equations [43].

$$a_i = a_o + \sum_{i=1}^{N} \Delta a_i;\ where\ \Delta a_i = C\left(\Delta K_{I(i)}^{A}\right)^m \Delta N_i \tag{55}$$

$$c_i = c_o + \sum_{i=1}^{N} \Delta c_i\,;\ where\ \Delta c_i = C\left(\Delta K_{I(i)}^{C}\right)^m \Delta N_i \tag{56}$$

$$N = \sum \Delta N_i \tag{57}$$

3 FEA Methodology and Modelling

The results generated as part of this thesis (stress intensity factors) were calculated on the basis of the FEA software package SimModeler Crack using displacement correlation technique. This section describes the 2D and 3D modeling approach used in FE based fracture analysis, however, the models used throughout this research were created and analyzed with the 3D modeling approach only.

3.1 2D FE-Based Fracture Analysis Methodology

The crack front is separated into elements along its length and the crack tip is discretized by quarter node, six-node triangular elements (Figure 16).

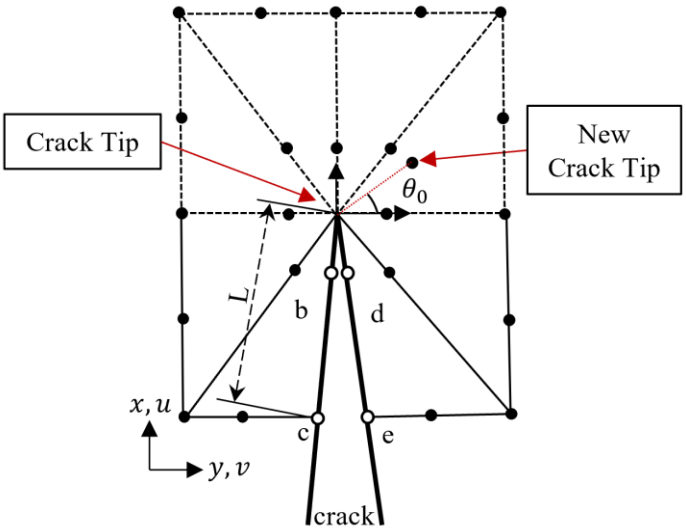

Figure 16 - Typical 2D crack tip discretization using triangular quarter-point elements [44].

Shape functions are used to calculate nodal displacement, the displacement values are then employed to calculate stress intensity factors [44]:

$$K_I = \frac{G}{\kappa + 1}\sqrt{\frac{2\pi}{L}}[4v_d - v_e - 4v_b + v_c] \tag{58}$$

$$K_{II} = \frac{G}{\kappa + 1}\sqrt{\frac{2\pi}{L}}[4u_d - u_e - 4u_b + u_c] \tag{59}$$

Where ν is Poisson's ratio, L is the element length at the crack tip, u_i and v_i are displacements in the x and y directions of nodes b, c, d, e, G is the shear modulus and $\kappa = (3-\nu)/(1+\nu)$ for plane stress and $\kappa = (3-4\nu)$ for plane strain [44]. For mixed mode applications the effective stress intensity factors can be combined as shown in Eq. (60):

$$K = \sqrt{(K_I^2 + K_{II}^2)(1-\nu^2)} \tag{60}$$

Direction of crack propagation is calculated at every crack increment. The maximum tangential stress criterion (MTS) [45] is used to advance the crack front radially in the plane perpendicular to the direction of greatest tension [46]. The crack increment is predefined within the simulation parameter, only the crack propagation angle (θ_0) is calculated using the equation below:

$$\theta_0 = 2tan^{-1}\left[\frac{1}{4}\frac{K_I}{K_{II}} \pm \sqrt{\left(\frac{K_I}{K_{II}}\right)^2 + 8}\right] \tag{61}$$

3.2 3D FE-Based Fracture Analysis Methodology

In the three-dimensional approach the crack tip and crack edge shown in Figure 16 were replaced with a crack front and crack face. Barsoum [47] demonstrated that the displacement method could be used with three-dimensional twenty-node cubic element with four mid-side nodes at the quarter points or with three-dimensional prism with four mid-side nodes at the quarter points (degenerate cube with one face collapsed). Ingraffea and Manu [48] generalized the correct stress intensity factor computational scheme for three-dimensional models for cases where geometry and/or loading are unsymmetric and the crack surfaces are unrestrained:

$$\begin{aligned} K_I = \frac{E}{4(1-v^2)}\sqrt{\frac{\pi}{2}}L_1[&2v_B - v_C + 2v_E - v_F + v_D - 2v_{B'} + v_{C'} - 2v_{E'} + v_F - v_{D'} \\ &+ \frac{1}{2}\eta(-4v_B + v_C + 4v_E - v_F + 4v_{B'} - v_{C'} - 4v_{E'} + v_{F'}) \\ &+ \frac{1}{2}\eta^2(v_F + v_C - 2v_D - v_{F'} - v_{C'} + 2v_{D'})] \end{aligned} \tag{62}$$

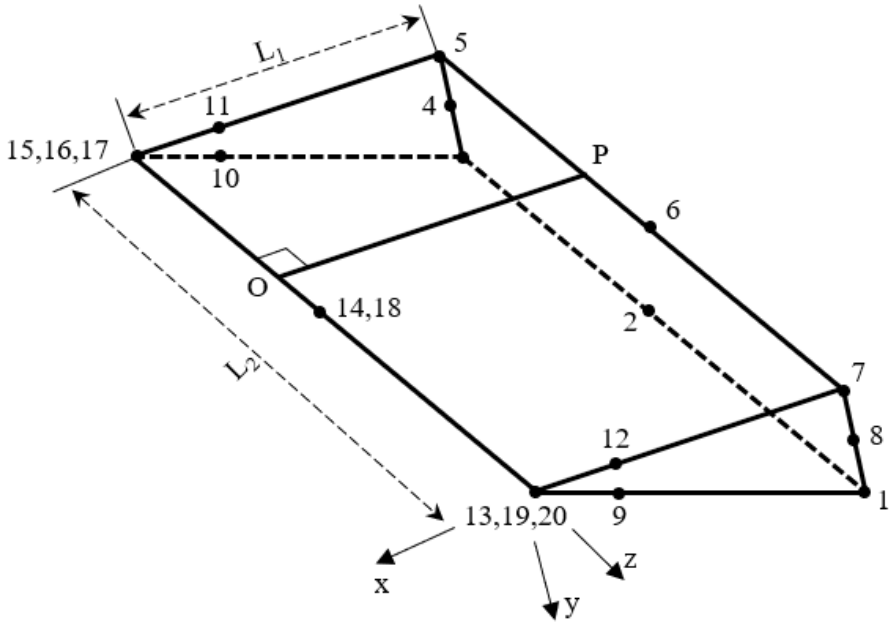

Figure 17 – Collapsed quarter-point wedge used in meshing of 3D crack geometry [48].

Figure 17 depicts a single wedge element with the associated nodal numbering and coordinate system used in 3D FE crack propagation simulations. Line L_2 is the collapsed face of a 20-node brick element. Equation (62) uses two quarter-point wedge elements united along L_2 to form the crack front and separated such that two crack faces are formed between the two wedges as shown in the figure below. Figure 18 presents two wedge elements forming a portion of the crack front.

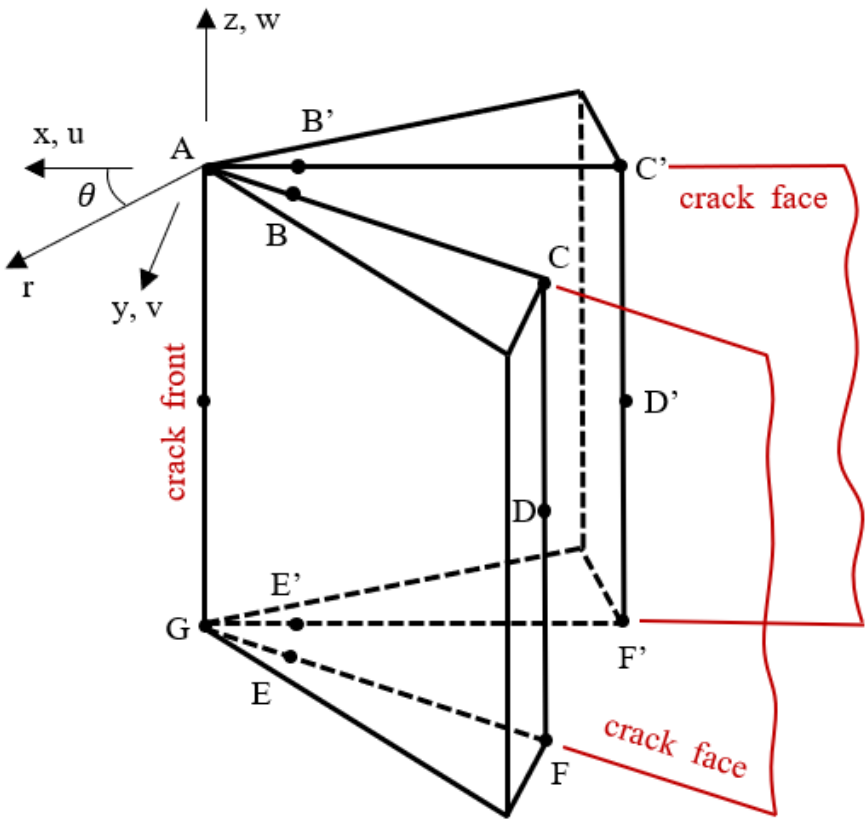

Figure 18 – Typical arrangement of wedge element along a portion of the crack front [48].

For a complete derivation of K_I, K_{II}, K_{III} as it applies to 3D FE fracture analysis, the reader is directed to the works published by Barsoum [47], and Ingraffea and Manu [48].

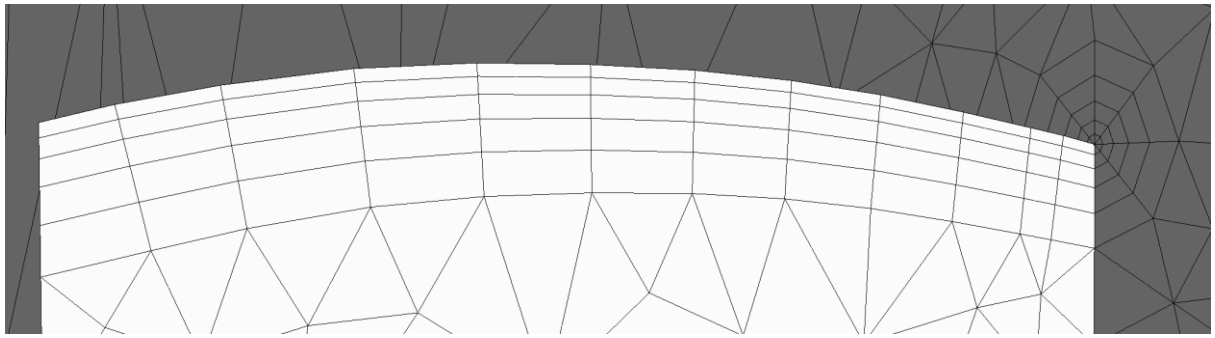

Figure 19 - Typical 3D FEA crack front discretization.

3.3 FEA Methodology

The three-dimensional (3D) FE models for the plate, multi flaws plate(s) and spar were built using SimModeler Crack. The SimModeler Crack software package can be used as a pre-processing tool to manipulate CAD models, generate fully customizable mesh, produce run-ready crack propagation input for solvers and a post processing tool that can be used to analyze crack growth behaviour. A pristine CAD model was imported, after which an initial crack geometry was defined and inserted in the main model. The FE meshing, pre-processing and post-processing operations were performed with the SimModeler software package. Crack configurations will be discussed in more detail in the sections below. Post processing was performed through SimModeler using displacement correlation technique for stress intensity factor calculation and maximum tangential stress criterion to solve for crack growth direction and effective ΔK. The sequential 3D crack growth technique as used in SimModeler has five distinct modeling process steps [49]:

i. Loading of CAD model
ii. Specified boundary conditions (boundary conditions, loading)
iii. Crack domain (Crack insertion and local remeshing)
iv. Model solution and postprocessing for stress intensity factor calculation
v. Incremental crack advancement and model update Figure 3 shows the SimModeler fatigue crack growth modelling process.

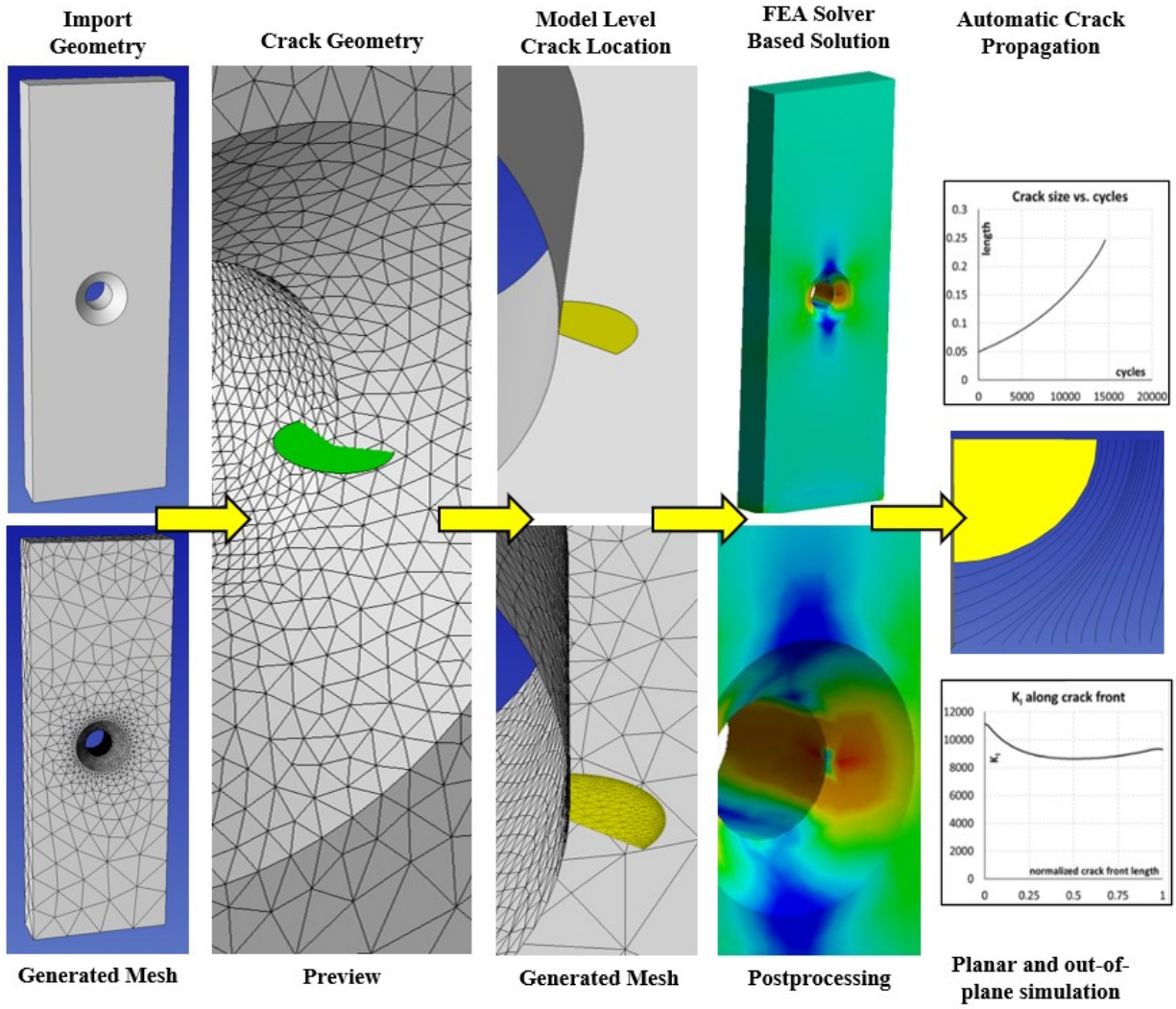

Figure 20 - Typical corner crack at a hole example. 3D explicit crack advancement modelling procedure in SimModeler.

Figure 21 describes the typical steps that are part of the preprocessing stage. In SimModeler, a set of attributes can be associated with the geometric entities (edges, faces, vertices) to assign meshing related parameters (mesh size on different geometric entities, mesh gradation etc.) or analysis features (boundary conditions, material properties). This association is persistent throughout the entire fatigue crack growth simulation. A crack can be defined in the traditional way (elliptical. rectangular or a combination) or, a CAD surface can be used to define any crack geometry. The fatigue crack growth analysis is performed on the model containing the crack (cracked FEA model).

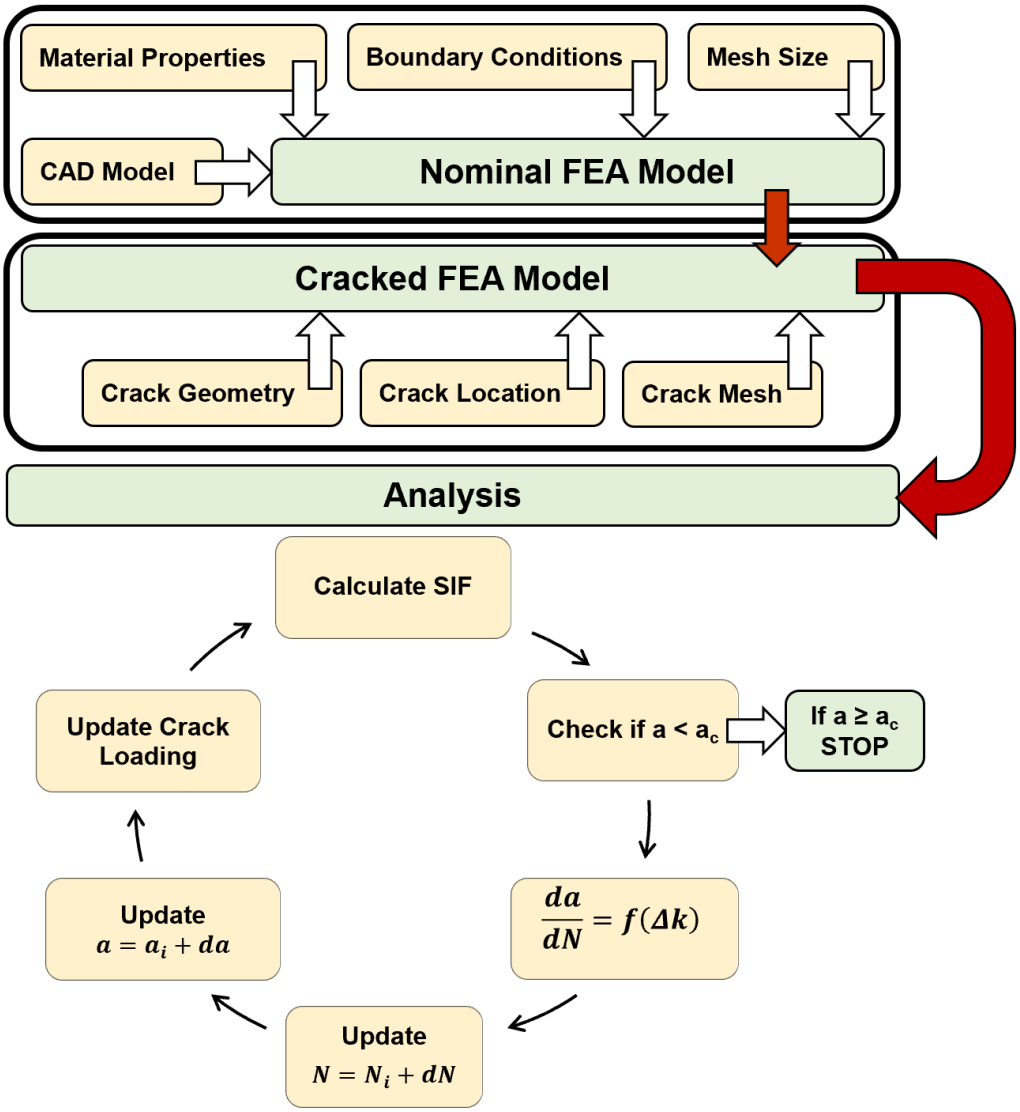

Figure 21 - Typical methodology in 3D FE based fatigue crack propagation.

Typically, during the analysis, the solver will calculate the SIF values based on the initial conditions (crack size and boundary conditions). For each crack growth increment a check is performed to ensure that the crack size is below the critical value otherwise the simulation stops. In the next step, SimModeler Crack calculates *delta N* by integrating the Paris equation using a fixed value of *da*. Crack shape and direction are incremented using the results of the previous step. Crack parameters and loading conditions are updated in order to solve the new model and calculate a new set of SIF values.

3.4 Single Flaw Model

A plate geometry as shown in Figure 22 was used to generate 3D FE crack growth results for three different crack configurations as depicted in in Figure 19. Ti-6Al-4V was used as the baseline material for both the FE and analytical crack growth studies, the material properties used in the analysis are shown in Table 1. The plate model has dimensional features of 96 mm in length, 48 mm in width and 16 mm thick. The three crack configurations used in this research were chosen on the basis of the available approximate analytical solutions [50], [51], [52], [53]. Initial crack geometry and aspect ratio was selected on the recommendations provided in [32], [40], consisting of an elliptical shape with a semi-minor axis of 2 mm (a) and a semi-major axis of 3 mm (c).

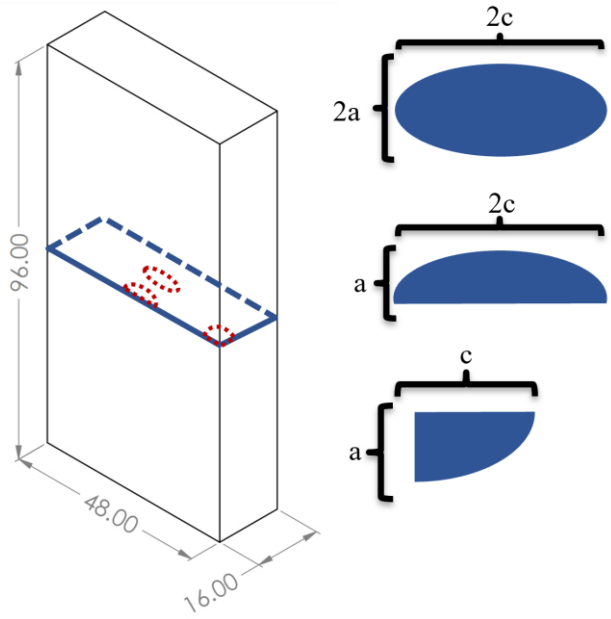

Figure 22 - Plate model with three crack configurations used to generate 3D FEA crack growth data.

Table 1 - Plate model material properties [54].

Parameter	Value
Alloy	Ti-6Al-4V
Young's Modulus	115 GPa
Poisson's Ratio	0.33
C coefficient (Paris)	1.77e-14 MPa$\sqrt{\text{mm}}$
m exponent (Paris)	3.667

The crack was inserted at a height of 48 mm, at the center of the plate; relative position of the surface semi-elliptical and quarter-elliptical crack with respect to the middle plane as presented in Figure 23. The model was constrained to prevent rigid body motion and a uniform tensile load was applied across the top surface. The semi-elliptical surface crack configuration was modeled using remote stress values between 50 MPa to 200MPa in 25 MPa increments and R ratio of 0.

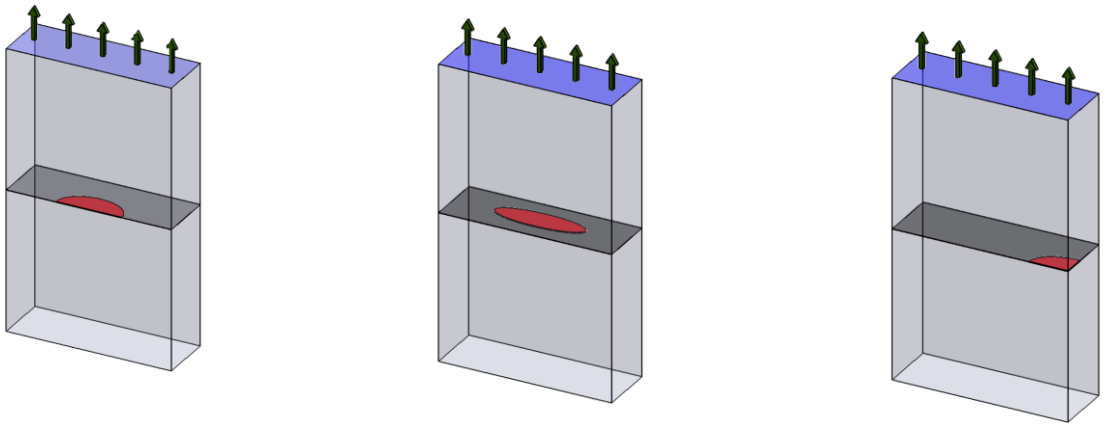

Figure 23 - Plate model configurations, crack location and boundary conditions.

The embedded elliptical and quarter-elliptical were modeled at a single applied loading of 200 MPa. The fully meshed and pre-processed model parameters are shown in Table 2.

Table 2 - Plate Model FEA Parameters.

Parameter	Value
Uniform Tensile Load	200 MPa
Material Model	Isotropic Linear Elastic
Ansys Mesh Element	Solid 186, Solid 187, Solid 185
Crack Propagation	Planar growth Mode I based

The models were meshed with three distinct element types [55]:

- Solid185: 3-D 8-Node Structural Solid, each node has three degrees of freedom (translation in nodal x, y and z directions). The element type is able to undergo plasticity, hyperelasticity, stress stiffening, creep, large deflection and large strain. It can be degenerated based on model requirements into a prism, tetrahedral or pyramid.

- Solid186: 3-D 20-Node Structural Solid, each node has three degrees of freedom (translation in nodal x, y and z directions). The element type is able to capture and output plasticity, hyperelasticity, stress stiffening, creep, large deflection and large strain. It has geometry degeneration options for tetrahedral, pyramid or prism.
- Solid187: 3-D 10-Node Tetrahedral Structural Solid, each node has three degrees of freedom (translation in nodal x, y and z directions). The element type is able to detect and output plasticity, hyperelasticity, stress stiffening, creep, large deflection and large strain.

3.5 Multiple Flaw Model

The 3D FE approach was further tested by simulating crack propagation in specimens containing multiple flaws and compare numerical solutions to the experimental measurements in terms of crack propagation life and crack path [41] for modeling validation purposes. In the experimental procedure, specimens made of Aluminium 2024-T3 were used. Table 3 contains the parameters of the isotropic linear elastic constitutive model used in the 3D FEA. Two nominal specimen geometries were imported into SimModeler and cracks were inserted around the fastener holes representative of the two different crack configurations namely 3F02 and 4F02 (reference) as depicted in Figure 24. A total of five 1 mm edge cracks were placed around the through holes at an angle of 45° with respect to the longitudinal axis of the samples. The FE model parameters are presented in Table 4.

Table 3 - Multiple Flaw Specimen Material Properties [41].

Parameter	Value
Alloy	Al2024-T3
Young's Modulus	73.1 GPa
Poisson's Ratio	0.33
C coefficient (Paris)	1.18e-12 MPa$\sqrt{\text{mm}}$
m exponent (Paris)	3.2

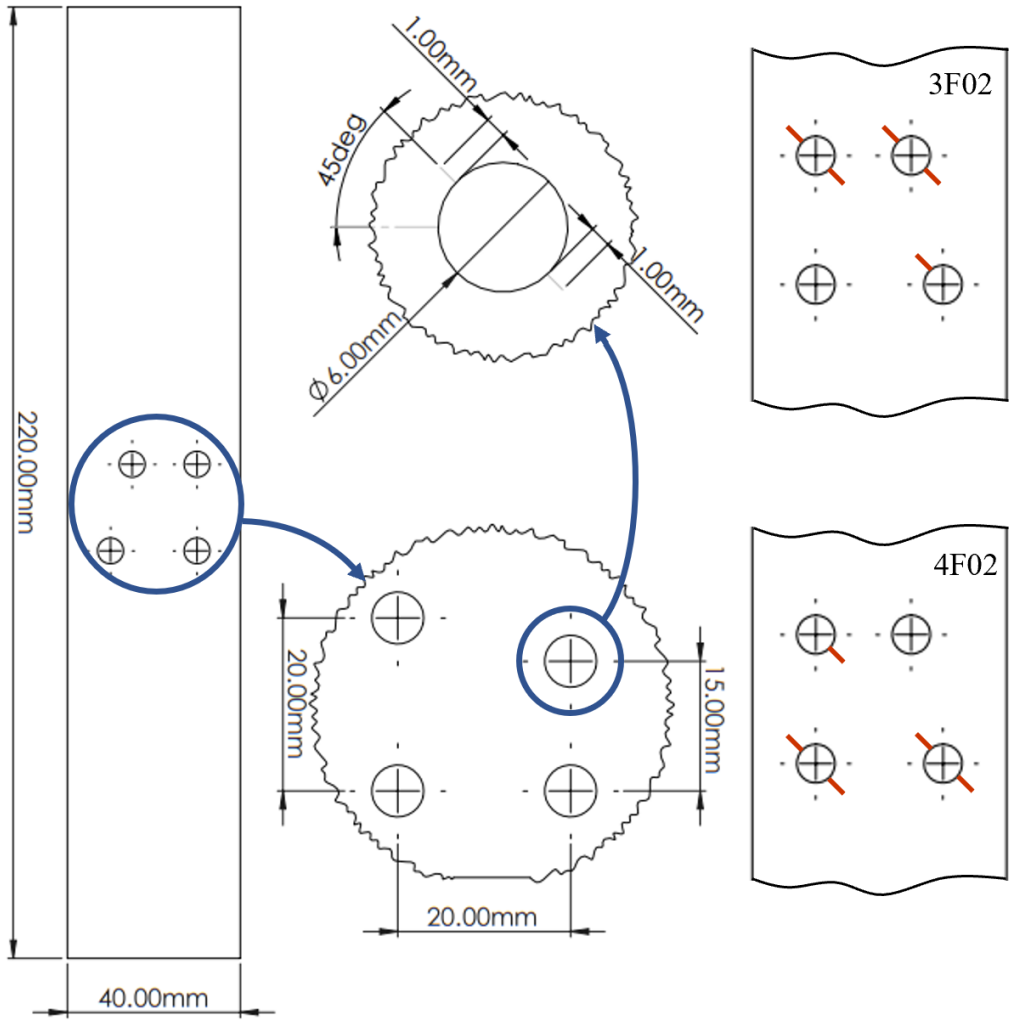

Figure 24 - Two configurations of the multi-damage panel.

Nodal constraints were applied on the FE model to prevent rigid body motion and tensile uniform load of 47.15 MPa was applied on the top and bottom model faces (Figure 25). The loading cycle applied to the 3D FE model was representative to the experimental loading conditions.

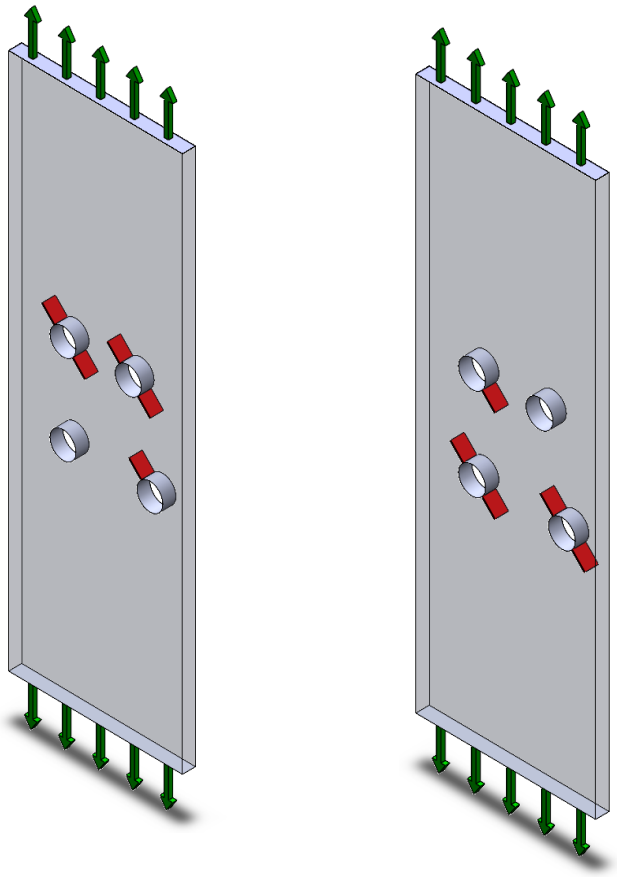

Figure 25 – Boundary conditions for simulated multiple flaw specimens.

Table 4 - Multiple Flaw Specimen FEA Model Parameters

Parameter	Value
Uniform Tensile Load	47.15 MPa
Material Model	Isotropic Linear Elastic
Ansys Mesh Element	Solid 186, Solid 187, Solid 185
Crack Propagation	Out of Plane

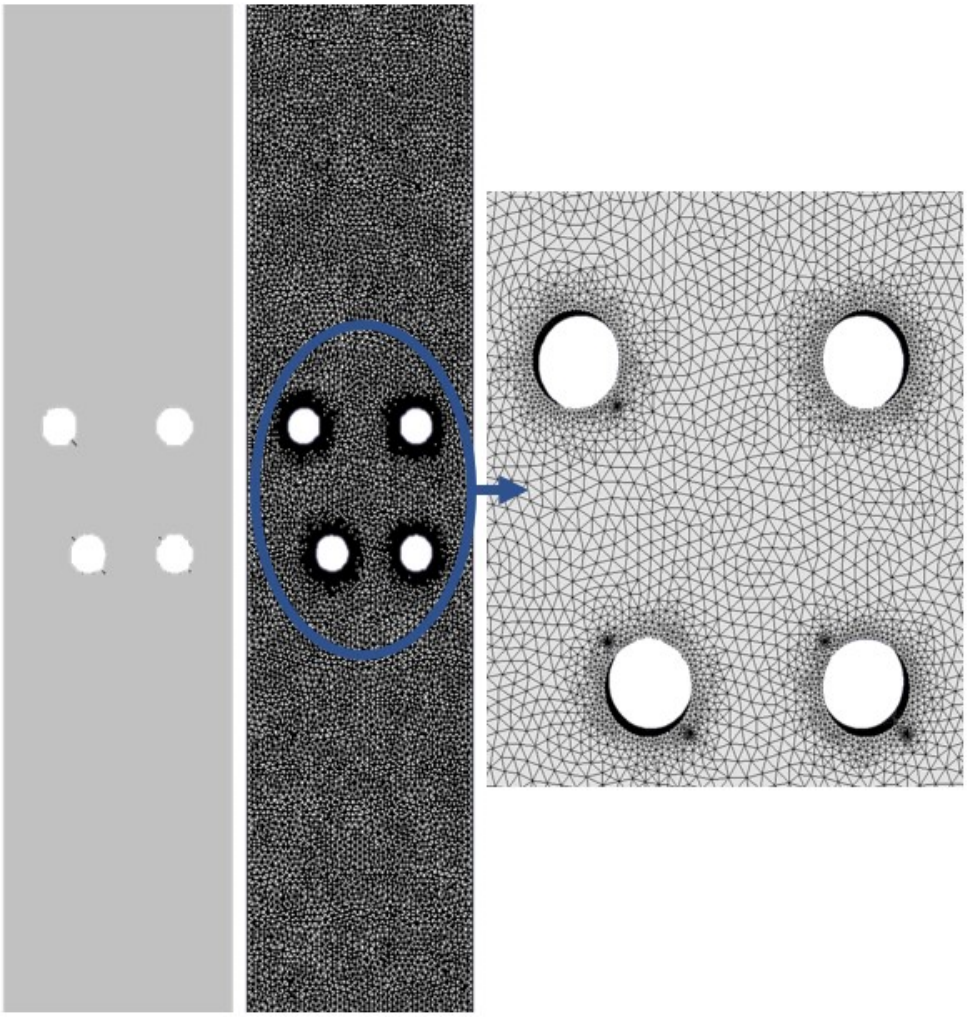

Figure 26 - 3D model used to represent panel geometry and predict crack propagation paths and remaining useful life.

The mesh element type capabilities were discussed in Section 3.2. A coarser mesh was selected for the bulk of the 3D model and a finer mesh was applied around the four holes in order to capture the curvature of the round features, as well as, ensure an accurate stress and strain solution.

Thin sheet aluminium specimens made of Al2024-T3 with multiple holes were tested experimentally under constant amplitude cyclic loads at a frequency of 1 Hz. The location of the holes and crack positions were chosen to measure fatigue crack growth lives and observe crack path interaction between multiple cracks [41].

3.6 Spar Model

As part of a wider program meant to implement standardized damage tolerance procedures that could make use of significant residual strength and stable crack growth life not accounted for with the original design methods, a full-sized spar was instrumented and fatigue tested until failure [42]. Figure 27 shows a complete spar, the top and bottom sections were fastened to the fatigue machine and subjected to pure tension constant amplitude loading. The experimental conditions were replicated in a 3D FEA model.

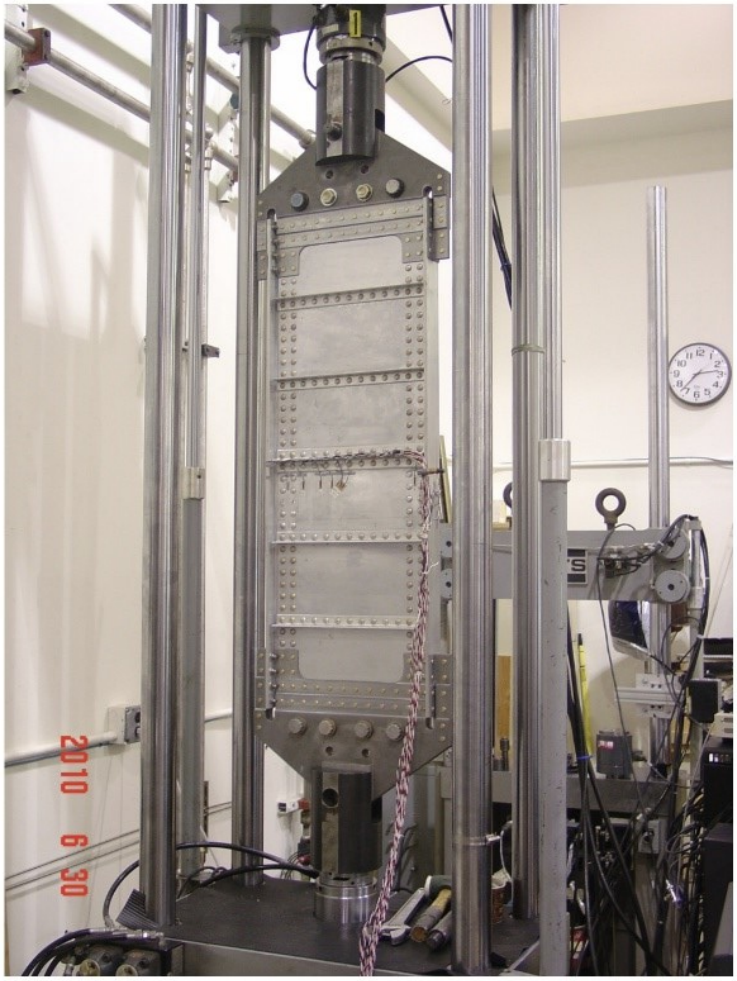

Figure 27 - Instrumented spar in fatigue stand [42].

The objective of the experiment was to characterize fatigue crack growth and crack path under pure tensile conditions. Test article materials and material properties were representative of typical A-10 center wing panel spar construction [42]. The top and bottom spar caps were made

from extruded 2024-T3511 aluminium riveted to the web constructed from 7075-T6 aluminium sheet. The spar caps were attached to the web through a double row of MS20470D8 protruding head solid rivets.

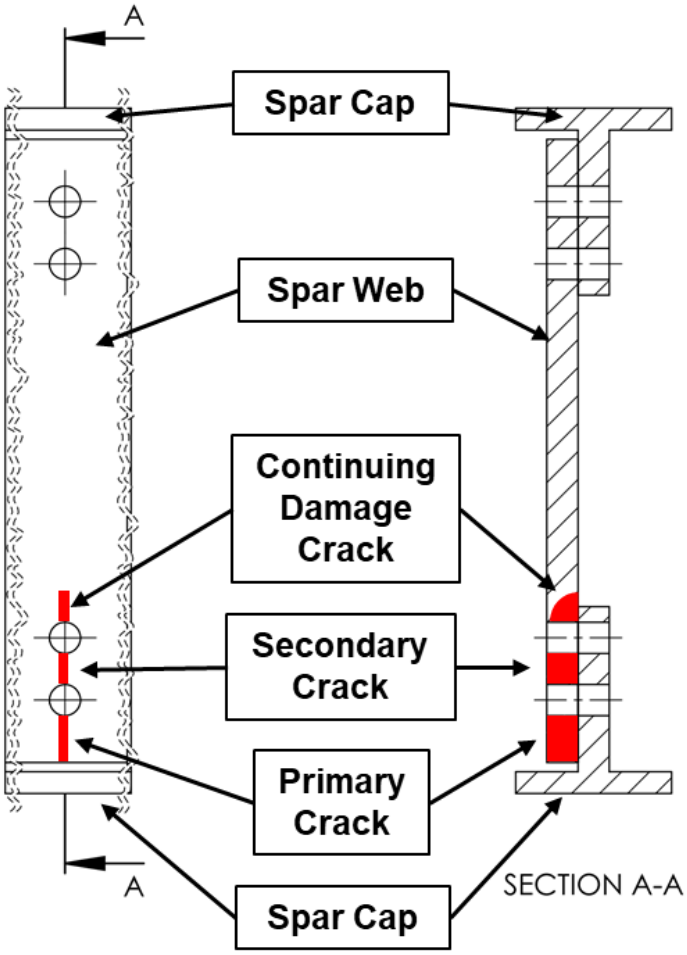

Figure 28 – Spar model and crack locations [42].

Each of the three cracks were tested separately in three distinct test stages. The cracks shown in Figure 28 were initiated under pre-crack test conditions from a 0.020 x 0.020-inch razor-cut at the rivet hole. Once the crack nucleated, the rivet hole was reamed and drilled to a diameter of 0.253 inch to 0.256 inch. The cracks were machined in undersized rivet holes in order to act like initiation sites for the crack, replicating similar flaws seen on in operation spars. After initiation, the hole was reamed to its standard size, thus, eliminating the time-consuming process of subjecting the spar to fatigue testing until the crack developed at the desired location. Initiated crack dimension for the cracks analyzed as part of the research are given in Table 5. The test was

conducted in three stages with crack 1 being initiated and propagated through the web, followed by crack 2 initiation and propagation, lastly the crack 3 was initiated and propagated through the entire width of the spar. Measurements of load cycles, crack growth and crack path were taken throughout the experiment.

Table 5 - Crack Dimensions

Sim Geometry	Sim Dimension	Experimental Crack
Crack 1		
Length Radius	0.05 in	0.02x0.02 in razor cut pre-cracked to 0.05x0.05 in
Height Radius	0.05 in	
Crack 2		
Length Radius	0.07 in	0.02x0.02 in razor cut increased to 0.07x0.06 in
Height Radius	0.06 in	
Crack 3		
Length Radius	0.04 in	0.04x0.04 in razor cut
Height Radius	0.04 in	

A simplified CAD geometry of the web and spar caps was used for the FE simulations (Figure 29). The spar model was 42 inches long and 15 inches wide, it contained two rows of five rivet holes without any fasteners. The numerical solution did not constrain the crack to grow in a planar mode since out of plane crack growth was observed during the experiment. Based on the experimental procedure the spar caps were not subject to crack propagations, as such, the decision was taken to analyze only the spar web with the 3D FEA methodology. A static analysis was performed on the spar web to determine the remote tensile stresses equivalent to the experimental loading setup. A fixed boundary condition was applied on the face at x = 0 in and a tensile force of 56 kips (249.1 kN) on the face at x = 42 in (Figure 31 - b). The upper and lower spar caps were bonded to the web. Gross section stress was measured at approximately 15 ksi (103.4 MPa) replicating the experimental conditions (Figure 31 - a). A static analysis of the web (no spar caps) determined that an applied tensile force of 92 kN was necessary to create remote field stresses similar to those observed during fatigue testing (Figure 31 - b).

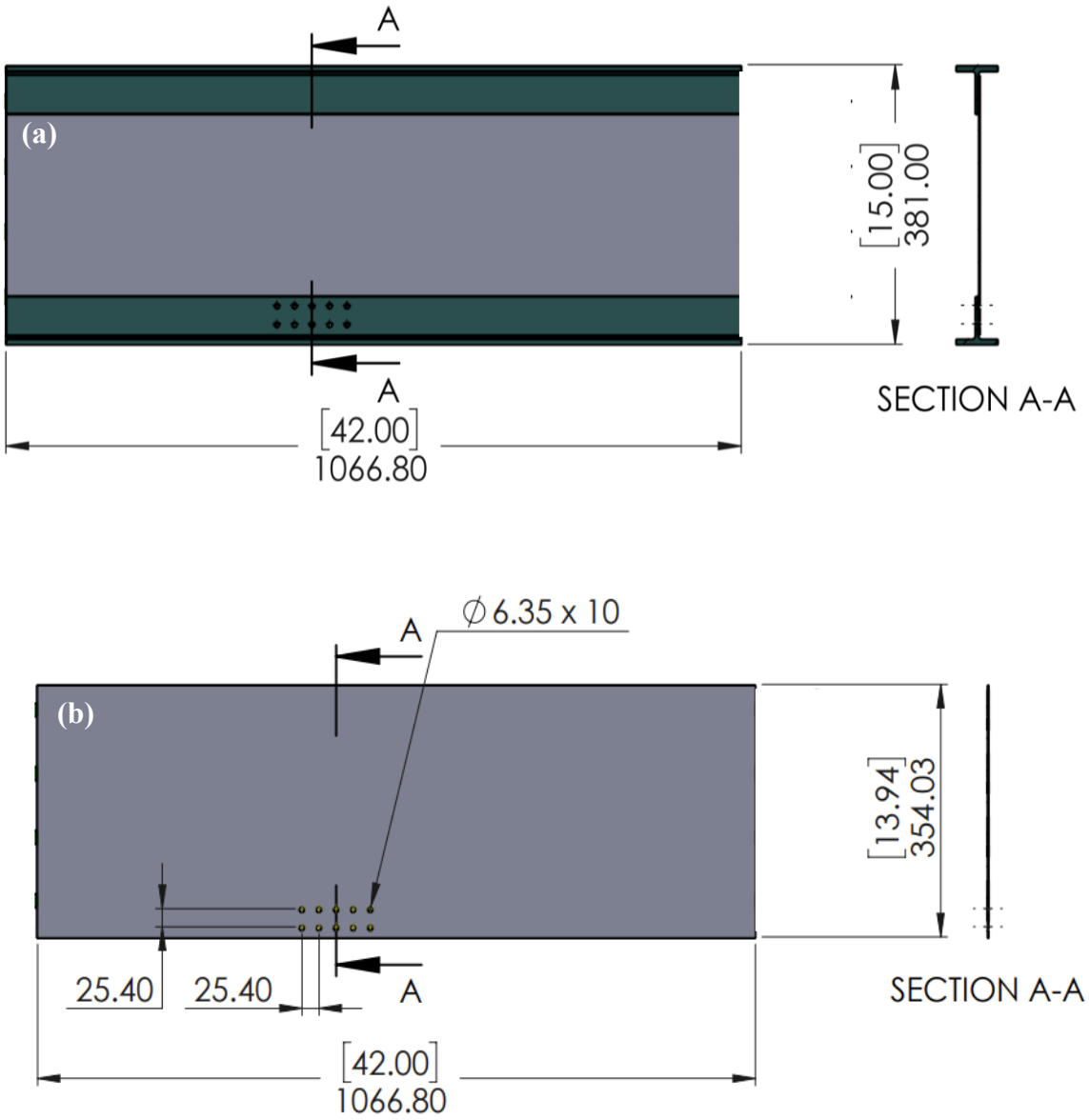

Figure 29 - Simplified spar (a), simplified web (b) geometry.

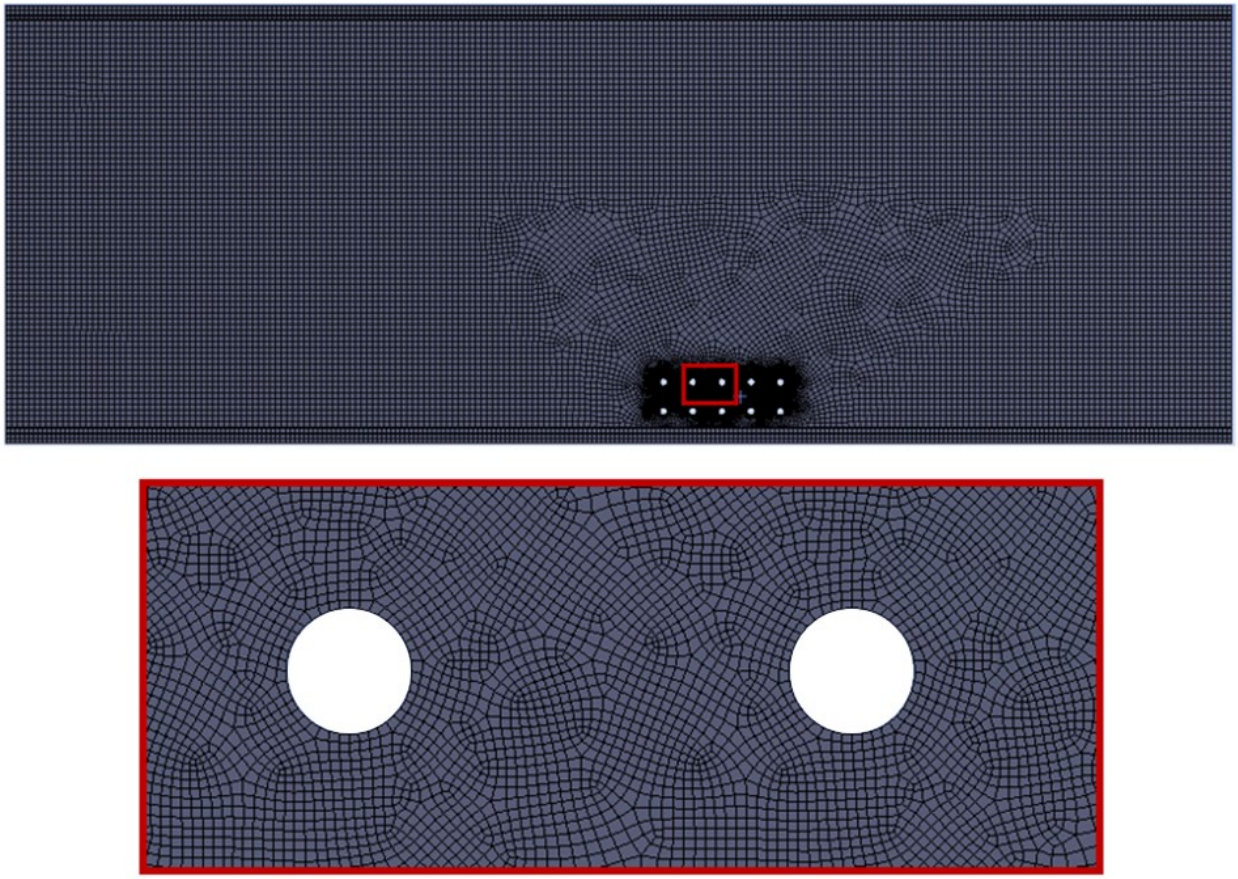

Figure 30 – Overall (top) and at the rivet holes(bottom) view of the solid mesh used in the simulations (no crack present in the model).

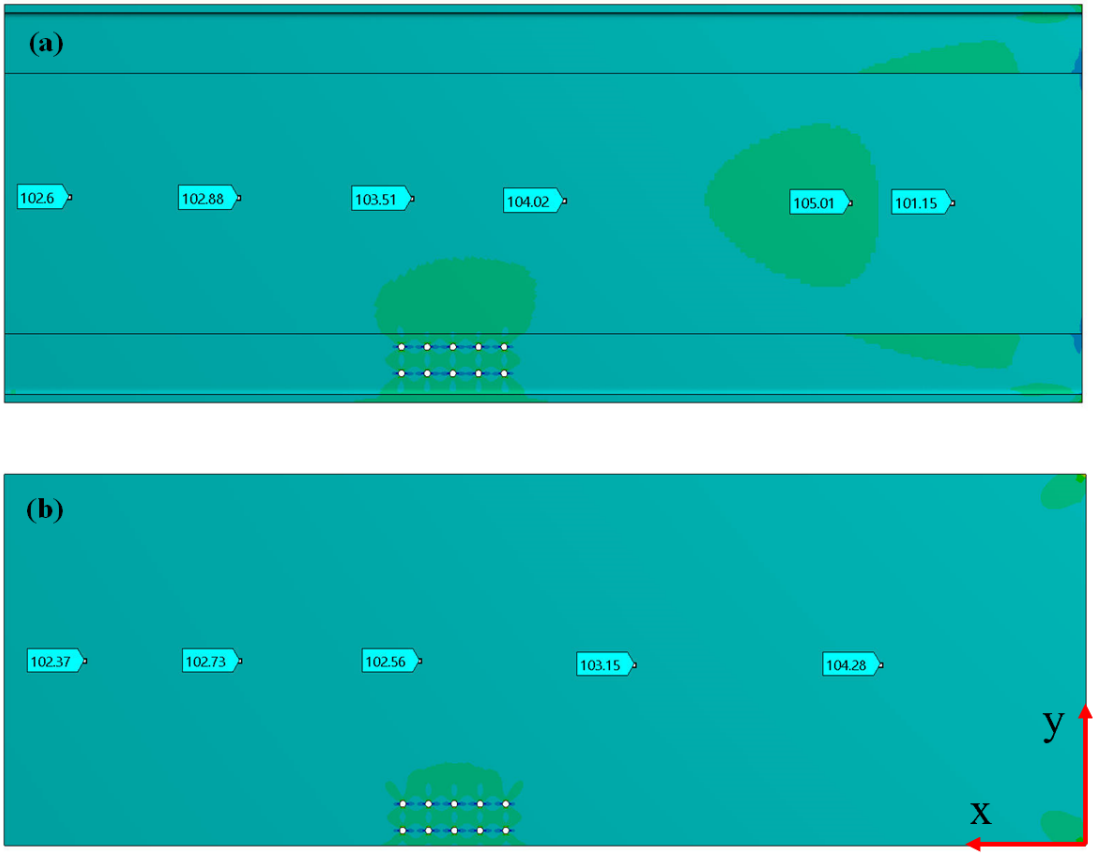

Figure 31 – Static analysis spar (a), web (b). Normal stress along the loading direction at different locations are shown for verification purposes.

The material properties associated with model are shown in Table 6. Boundary conditions were applied to prevent rigid body motion. The right-side face of the specimen was subjected to a 102.3 MPa uniform tensile load, equivalent to the 92 kN force determined in the static analysis. Crack propagation was set to mixed-mode to capture eventual out of plane behavior. Each of the cracks presented in Table 5 was simulated individually. Two new CAD models containing a 0.1 in slot were used in the crack 2 and 3 simulations. The slots were there to represent the fully propagated crack 1 and 2 respectively.

Table 6 - Spar Material Properties.

Parameter	Value
Alloy	Aluminum 7075 T6
Young's Modulus	71.7 GPa
Poisson's Ratio	0.33
C coefficient (Paris)	1.048e-12 MPa$\sqrt{\text{mm}}$
m exponent (Paris)	3.21

Table 7 - Spar FEA Model Parameters

Parameter	Value
Uniform Tensile Load	102.3 MPa
Material Model	Isotropic Linear Elastic
Ansys Mesh Element	Solid 186, Solid 187, Solid 185
Crack Propagation	Out of Plane

Based on preliminary fatigue life results and crack path discrepancies several misalignment and variation of material properties were assessed to study variation of loading condition and material properties on crack growth life and crack path results. The modelling procedure, results of these studies and nominal configurations are discussed in the next section. A single test article was fatigue tested in tension due to the large scale and complex nature of the part, as such, it was not possible to account for variation of test conditions and material properties. A complete assessment of the FEA approach against the test results of the spar structure was limited due to the aforementioned reasons.

4 Results and Discussion

4.1 Single Flaw Plate

The first set of results presented in Figure 32, Figure 33 and Figure 34 compare the FEA approach (green) to the analytical model results (blue) for all three crack configurations in terms of crack shape evolution and fatigue crack growth life. The analytical semi-elliptical surface crack configurations compared well with the 3D FEA based results for all seven different load levels as it can be seen in Figure 32. The embedded elliptical and corner quarter elliptical layouts analysed with the 2D methodology showed comparable results with the FE approach (Figure 33, Figure 34). Crack length datasets plotted as a function of cycles, for all three cases, are displayed in the figures below. Verification requirements were satisfied by demonstrating good correlation between FE model results (at all stress levels) and analytical solutions in terms of crack shape evolution and crack growth life. Figure 32, Figure 33, and Figure 34 illustrate crack front behaviour and fatigue lives for all three crack configurations. The small difference between crack front shape, numbers of cycles and crack length was due to elliptical crack front shape constraint within the analytical formulation. There were no crack front shape constraints applied to the 3D FE based solution, whereas the analytical procedure used an elliptical crack front defined by two crack front points.

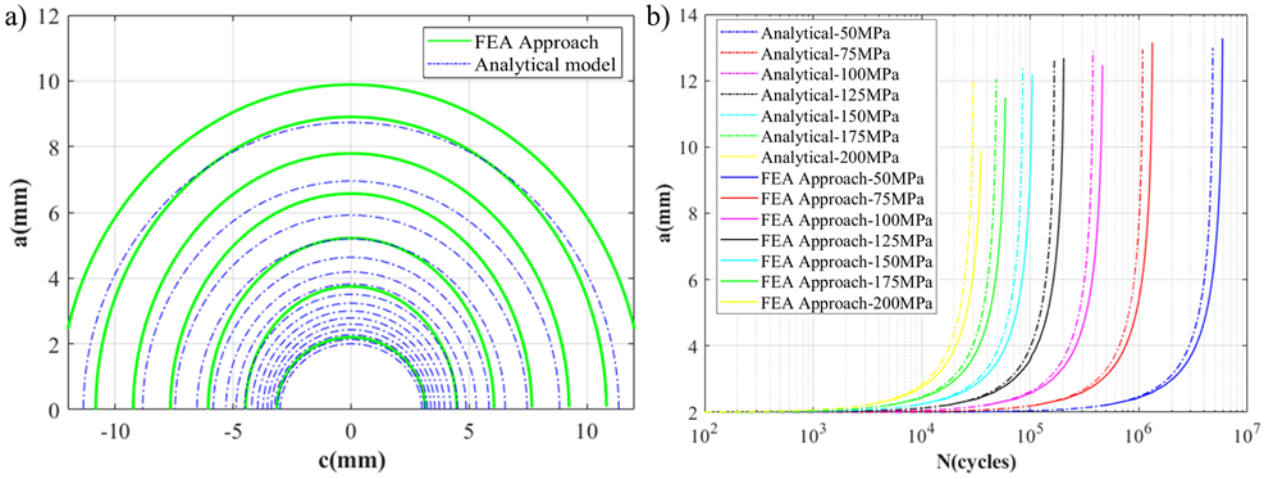

Figure 32 - Semi-elliptical surface crack analytical and FE results: a) crack shape evolution, b) fatigue crack growth life.

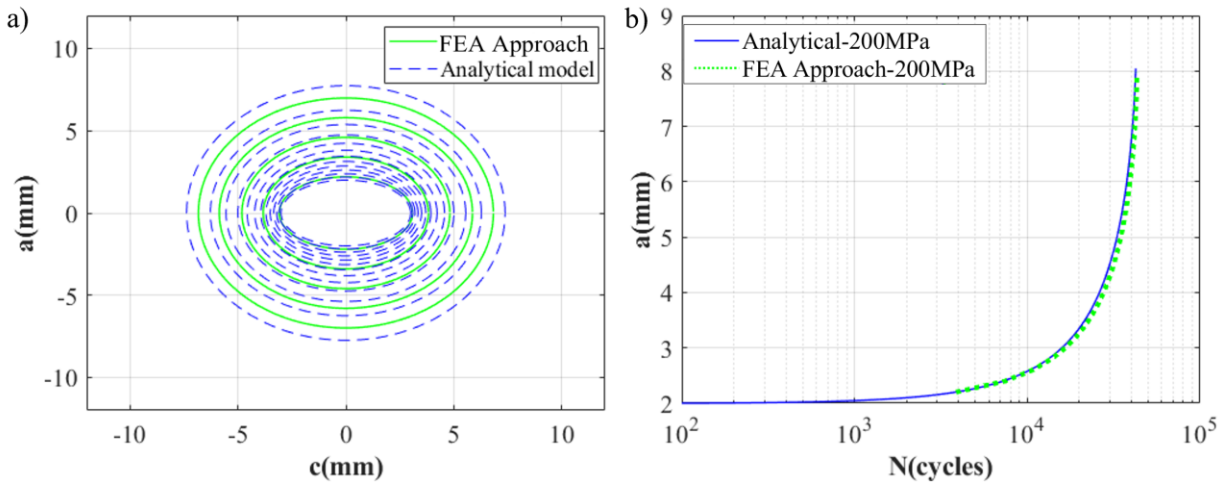

Figure 33 - Analytical and FE results for embedded elliptical surface crack: a) crack shape evolution, b) fatigue crack growth life.

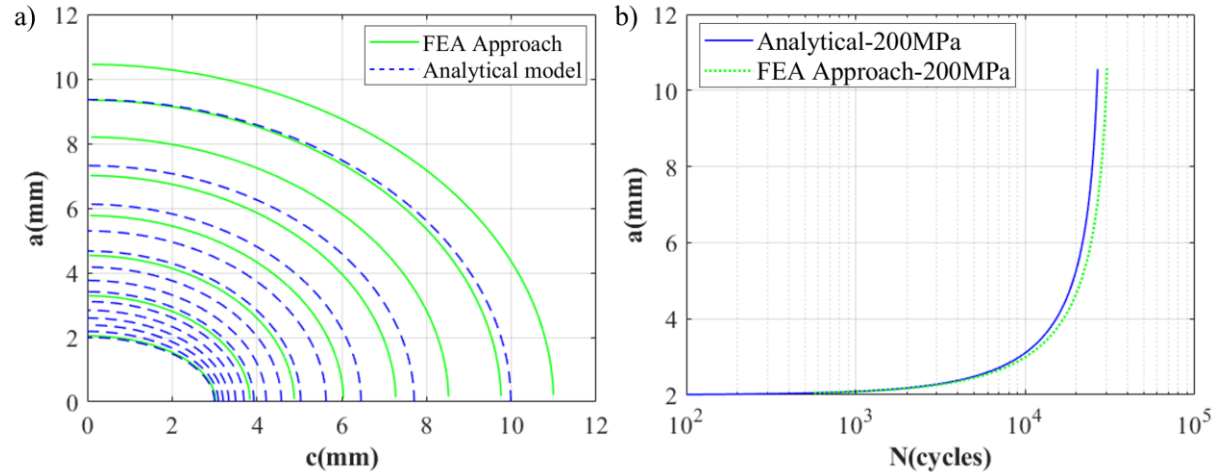

Figure 34 - Corner elliptical crack, analytical and FE results: a) crack shape evolution, b) fatigue crack growth life.

4.2 Multiple Flaw Plate

The multiple flaw study generated results for two specimen configurations presented in Figure 35 and Figure 36. The results shown compare crack path and fatigue lives between the SimModeler results (green) and the experimental data (grey). The FE model failure condition was at crack front reaching the edge of the specimen. The FE model and experimental results, consisting of crack

length and fatigue life data, showed good correlation as presented in Table 8 and Table *9*. Crack growth behaviour and fatigue life was in good agreement in both configurations and all five cracks. An overlay between experimental and numerical crack path propagation is shown in the figures below.

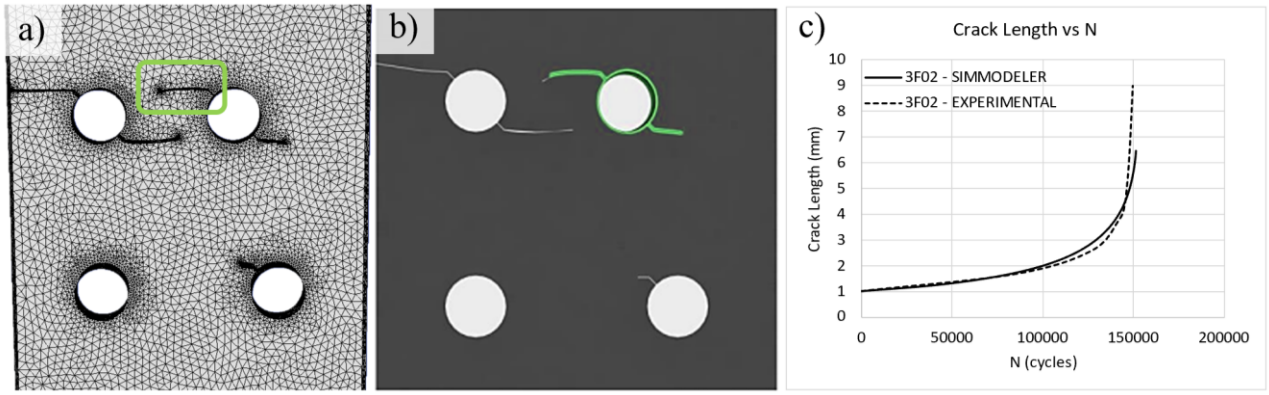

Figure 35 – Results overlay configuration 3F02 - crack 3 (SimModeler Crack results in green): a) snapshot of the crack path solutions from the 3D model; b) crack paths recorded in the experimental procedure overlayed the FEA crack path (green); c) crack length vs. cycles.

Table 8 – Fatigue crack growth life results configuration 3F02.

Analysis Type	Configuration	Cycles	Crack Length [mm]
SimModeler	3F02	151653	6.45
Experiment	3F02	149693	8.98

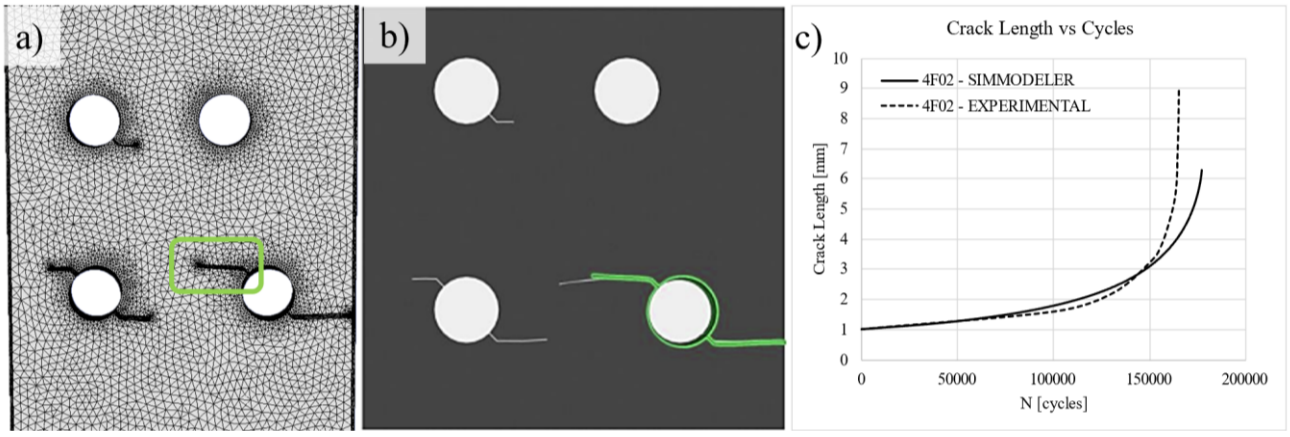

Figure 36 - Results overlay configuration 4F02 -crack 4 (SimModeler Crack results in green) a) snapshot of the crack path solutions from the 3D model; b) crack paths recorded in the experimental procedure overlayed the FEA crack path (green); c) crack length vs. cycles.

Table 9 - Fatigue crack growth life results configuration 4F02.

Analysis Type	Configuration	Cycles	Crack Length [mm]
SimModeler	4F02	177097	6.29
Experiment	4F02	165418	8.99

4.3 Spar Structure

4.3.1. Nominal Conditions

A set of crack growth simulations for crack 1, 2 and 3 configurations were conducted under nominal boundary conditions and material properties as described in Section 3.4. For crack 1 initiation site shown in Figure 37, initial flaw size was 1.27 x 1.27 mm. A load of 102.3 MPa was applied and directed along the long axis of the specimen. Failure in the lower ligament occurred at 20482 cycles. Crack behaviour followed expected planar mode I theoretical assumptions.

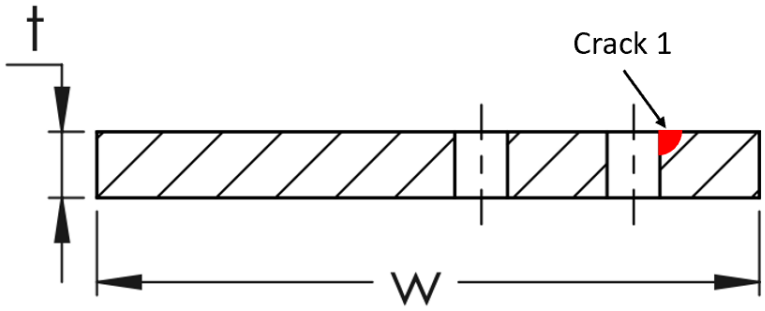

Figure 37 - Crack 1 initiation site.

The second crack was inserted as depicted in Figure 38. Crack 2 initial size was 1.778 (along the model face) x 1.524 (along the bore of the hole) mm. Nominal boundary conditions and material properties were applied. Fracture occurred after 2445 cycles. Crack 2 propagation path was normal to the applied tensile load.

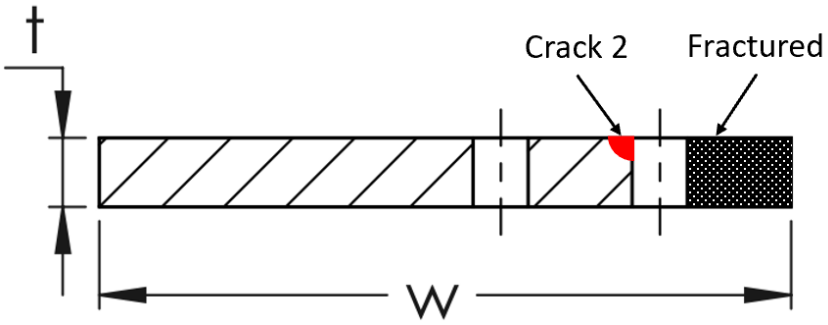

Figure 38 - Crack 2 initiation site and fractured crack 1.

The continuing damage crack was inserted at the second rivet hole with a size of 1.016 x 1.016 mm (Figure 39). As with the previous two cracks, the model used nominal material properties and boundary conditions as per Section 3.4. Crack 3 was propagated for a total of 88.7 mm and 1509 cycles.

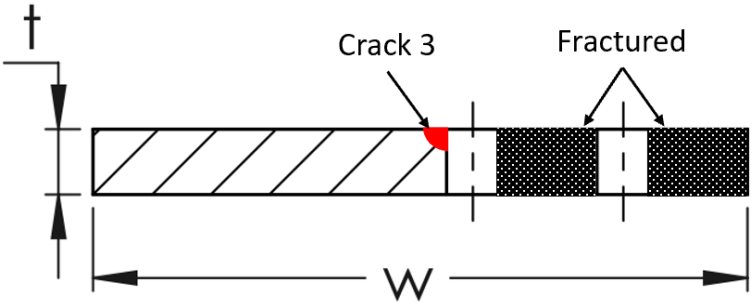

Figure 39 - Crack 3 initiation site and fractured crack 1 & 2.

Experimental and AFGROW results presented in [42] have been plotted along with simulated results obtained from the proposed 3D FEA approach in Figure 40. The AFGROW solutions shown below are under identical boundary conditions and material constants. Crack 1 behaviour is comparable with the experimental data showing similar crack growth length and numbers of cycles at fracture. However, crack 2 and 3 exhibit significant deviations from experimental data.

Table 10 - Crack growth cycles under nominal conditions.

	Cycles		
	Crack 1	**Crack 2**	**Crack 3**
Experiment	22378	7150	9400
AFGROW	36700	4149	1203
SimModeler	20482	2445	1509

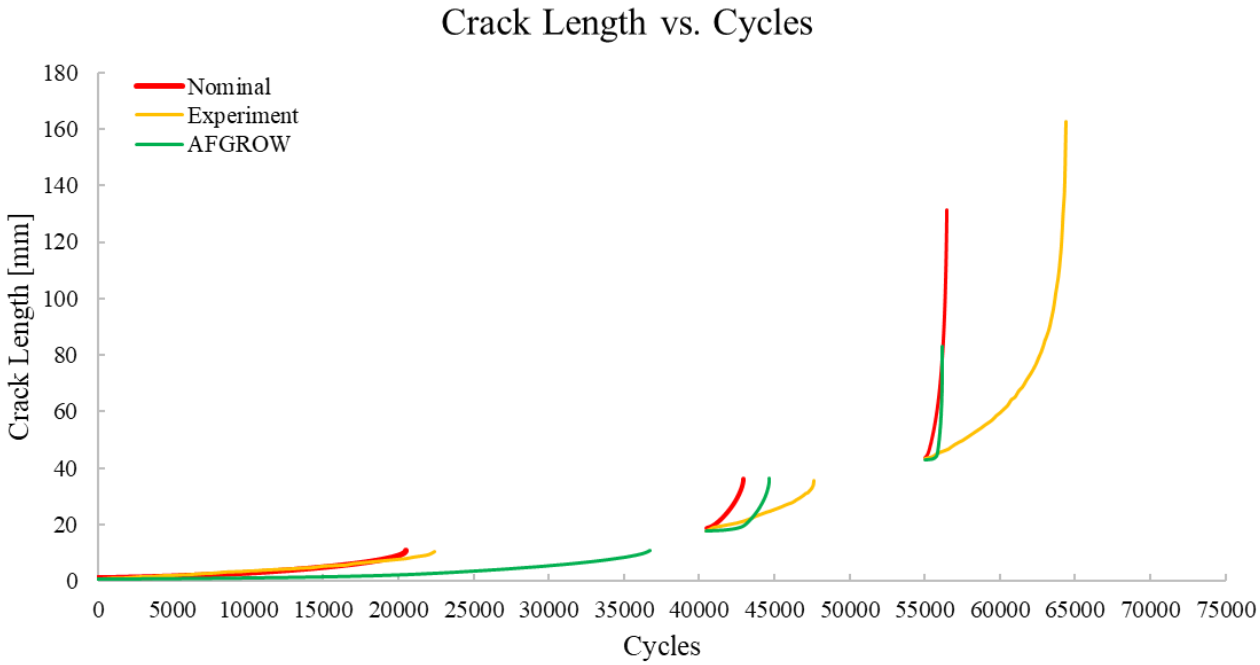

Figure 40 - Results for nominal boundary conditions and material properties.

Experimental crack path data collected during the spar fatigue test showed crack 3 deviating from theoretical predictions of a crack propagating under mode I tensile loads (for a typical plate like structure, crack path was expected to be a straight path in the normal direction of the applied uniform tensile load)., Figure 41 shows out of plane crack propagation. The adapted 3D FEA methodology generated a crack path in line with the theory i.e. crack propagation normal to the applied load, flat through the entire crack length.

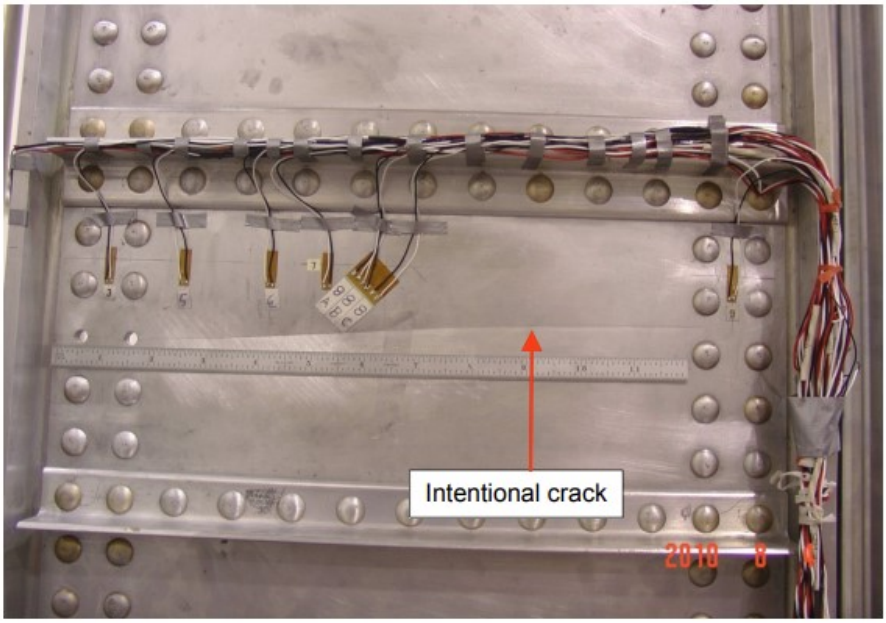

Figure 41 - Crack 3 experimental results [42].

4.3.2. Variation in Force Alignment and Material Properties

The large deviations in crack path and crack growth life shown in Figure 40 and Figure 44 between experimental and numerical data were further analyzed through alignment and material variation studies. During experimental testing an anomalous crack was discovered at 13762 cycles. It was located approximately 6 inches from the fatigue machine mounting bracket and measured approximately 6.56 inches in length. The repairs shown in Figure 43 consisted of a stop drill operation and installation of doubler plates. As a precautionary measure identical plates were installed at the opposite end of the spar [42]. A strain survey was subsequently performed which did not record any undesired effects from the repairs.

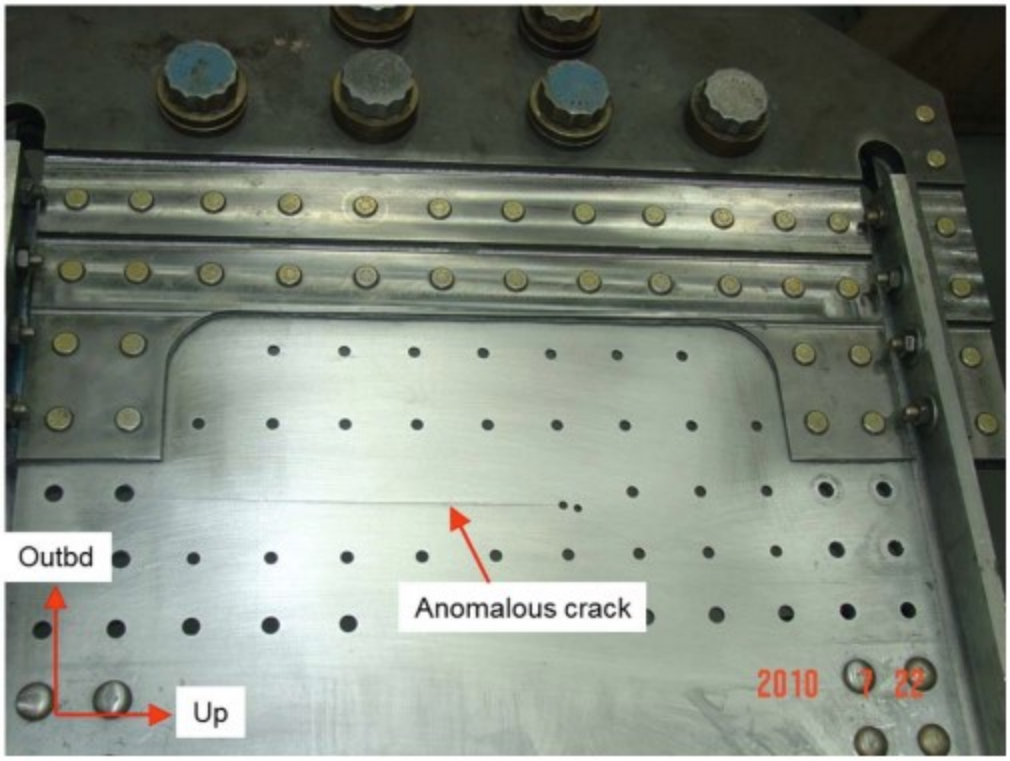

Figure 42 - Anomalous crack [42].

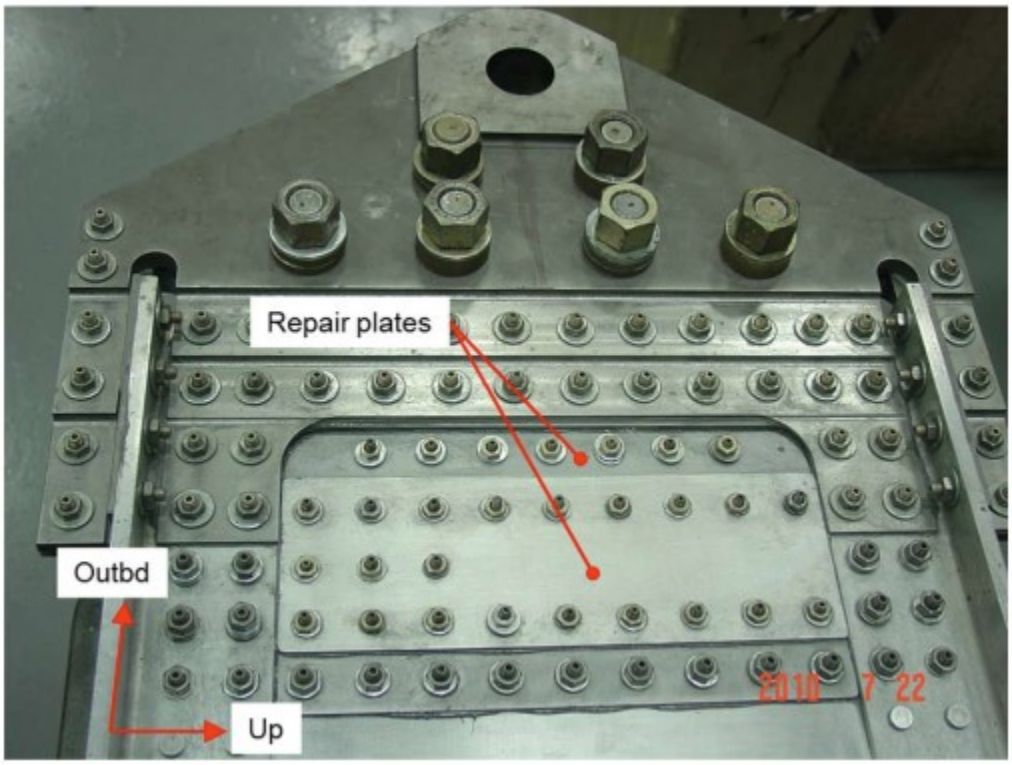

Figure 43 - Anomalous crack repair [42].

In order to evaluate the effect of the anomalous crack on the fatigue results recorded during the experiment, a numerical simulation was performed using a model which included the anomalous crack. A 0.1 mm slot was cut into the web at the same position as the crack discovered during testing. Boundary conditions and material properties were unchanged. For the same crack 3 length the number of cycles was 1520 with planar crack growth. The large difference in cycles and crack path remained unaccounted for.

Considering the lack of crack growth data ($da\,/\,dN - \Delta K$) of 7075-T6 specimens machined from the actual spar structure, a literature survey was undertaken to collect fatigue crack growth data for aluminium 7075-T6 reported by various studies. The goal was to provide an adequate explanation for the variation in fatigue life through variation of material crack growth properties. The original fatigue experiment did not confirm through extracted specimen data the material properties associated with that specific batch of aluminium, it simply stated that aluminium 7075-T6 was used in the construction of the web [42]. Fatigue crack growth data collected from a variety of sources was digitized and the Paris constants extracted from datasets are given in Table 11. Numerical simulations using baseline boundary conditions with the new material parameters (Paris constants shown in Table 11) were not successful in replicating the experimental results.

Table 11 - 3D FEA results using various Paris constants values.

CURVE ID	C	m
MMPDS	1.7165E-12	3.1269
USAF1	7.3373E-12	3.2086
USAF2	1.4146E-12	3.2154
USAFSHEET	3.0246E-12	3.0860
NASA2005	1.2153E-12	3.2216
NASA!CAE94!INCE1	5.0605E-12	2.9900
XIAOPING	1.7572E-12	3.1646
INCE2	2.6149E-12	3.086
INCE3	4.76E-12	3.0333
USEDinSIM	1.0488E-12	3.2100

An exploratory investigation was undertaken to ascertain the effect of misalignment on the numerical results and whether or not it could replicate the experimental results. The tested spar specimen was over one meter in length and 38 centimeters in width. Perfect alignment at the scale of the specimen would be difficult to achieve. A modified FEA model was created to vary the location where the tensile force is applied and its direction. Pilot nodes were inserted in the model to impart planar deviations from nominal applied force location as well as an angular difference for the tensile force direction. Seven scenarios were analyzed as shown in Table 12.

Table 12 - Misalignment Study Crack 3

Misalignment	Crack 3 [Cycles]
1° - 3 mm	3025
1° -6 mm	3571
2° - 3 mm	5707
2° - 6 mm	7090
2° - 10 mm	9543
3° - 3 mm	12760
3° - 6 mm	16586

Furthermore, the application of the above misalignments resulted in crack paths more representative of the experimental results. For simplicity not all crack path results are shown in the figure below. The 3° - 3 mm configuration showed the best correlation to the experimental crack path results. Even though, the 2° - 10 mm is a closer match in terms of cycles, a 10 mm misalignment was deemed too high not to be detected by the various experimental data collection tools.

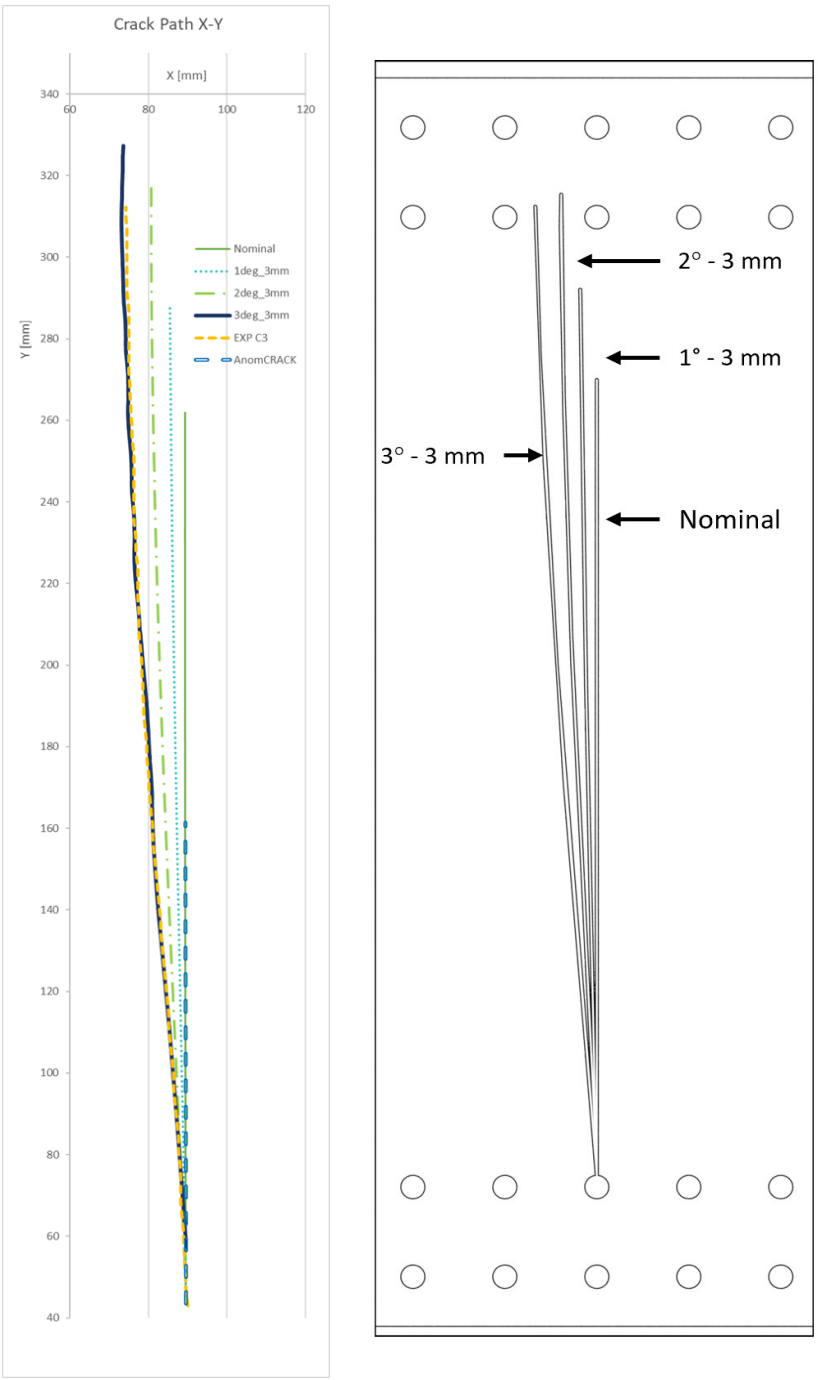

Figure 44 – Crack path results using various degrees of misalignment.

The digitized fatigue crack growth data [56] used to generate the Paris constants used throughout the simulations was processed to create a ± 30% variation in the nominal value of the $da\ /\ dN - \Delta K$ data points (Figure 45). It is assumed that during the manufacturing process of the materials used in the construction of the spar there could be instances where the mechanical and fatigue

properties vary from the nominal stated values. Since there was no mechanical and crack growth testing of the spar material performed to confirm the true mechanical and fatigue crack growth properties of the base material, the above-mentioned alternative was adopted to account for the variations of the material crack propagation behavior. The new crack growth constants were utilized to generate a full set of simulations results (crack 1, 2 and 3) that would account for potential variation in material crack growth behavior i.e. variation of Paris constants [57].

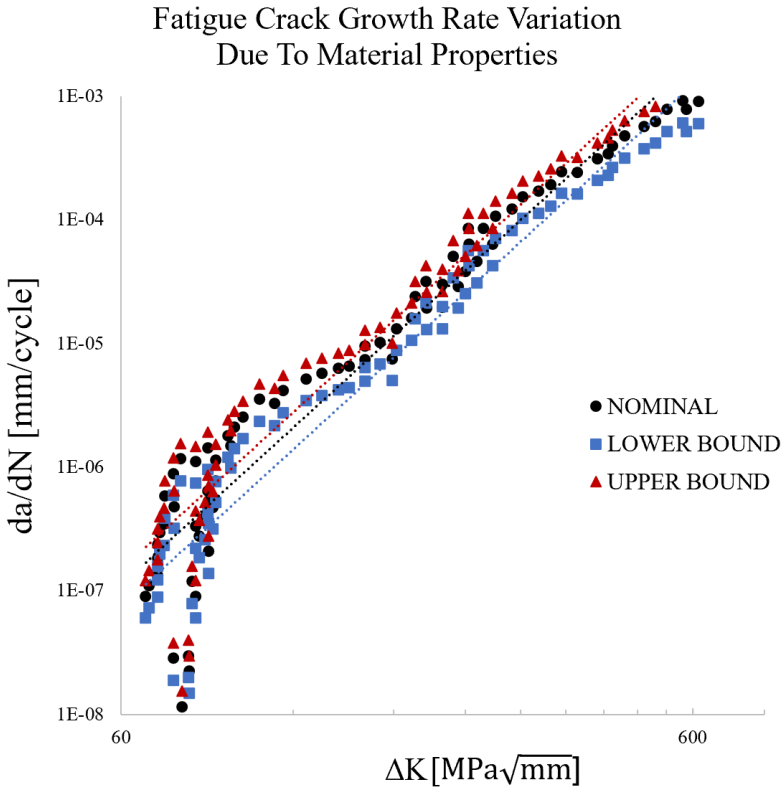

Figure 45 - Fatigue crack growth curves and calculated upper and lower bound.

Figure 46 shows the results of the material variation study. The material variation analysis was performed for crack 1 using nominal loading conditions, crack 2 using nominal loading conditions and crack 3 using a 3° - 3 mm load misalignment. The experimental measurements fall within the ± 30% range created by the lower and upper material properties bounds (generated by changing the C and m Paris constants and using a 3° - 3 mm misalignment configuration) centered on the 3° - 3 mm misalignment results with nominal Paris constants values (C=1.0488e-12 and m=3.21) (Figure 47).

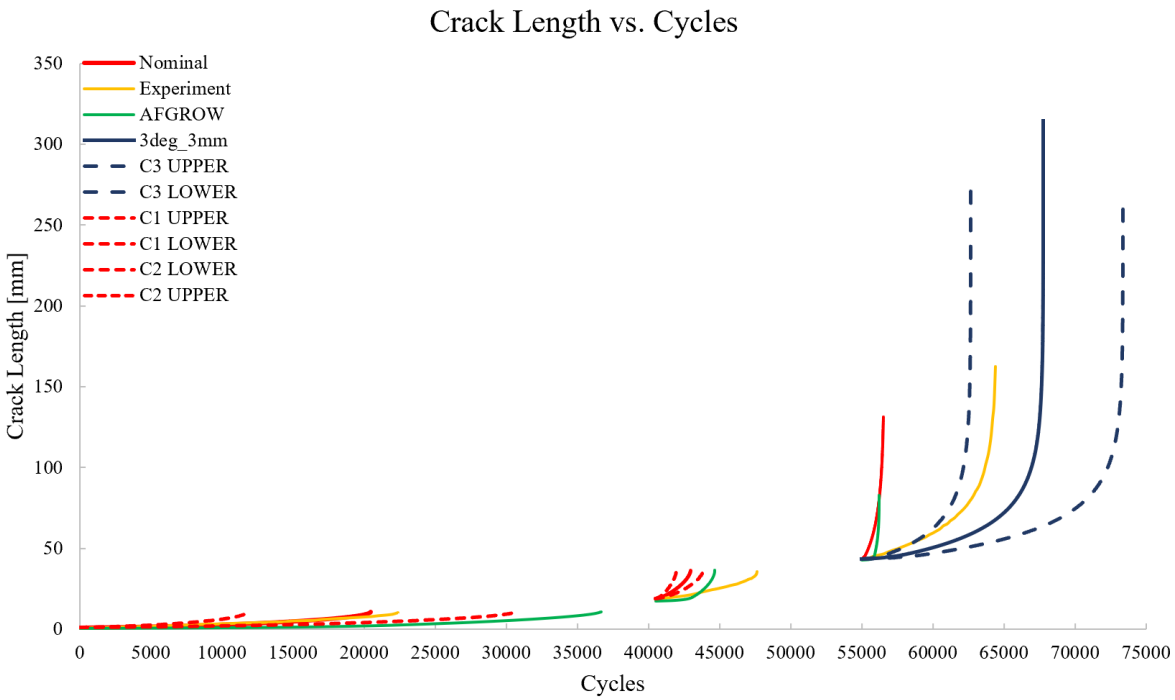

Figure 46 – Results for Crack 1, 2, 3 including material variation and misalignment study.

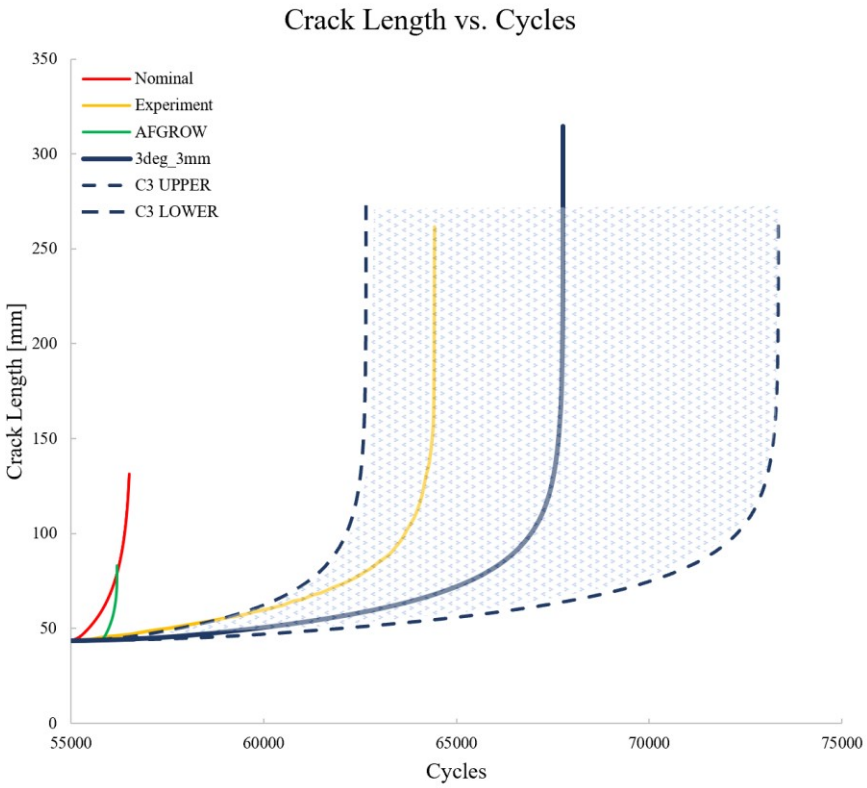

Figure 47 – Crack 3 results for material variation and misalignment study.

4.4 Summary

Fatigue crack growth results were generated based on a 3D FEA approach using the displacement correlation technique. The proposed method was verified and validated through analytical solutions and experimental data. The objective of the research was achieved in three main stages:

1. Verification of the 3D FEA based procedure was accomplished by comparing results of an analytical model to the numerical FEA generated crack path, shape and fatigue life for three different crack configurations and multiple load levels.

2. The 3D FEA based fatigue crack growth solutions were validated against experimental measurements carried in flat specimens containing multiple flaws. Remaining useful file and crack propagation path (out-of-plane) were used as validation criteria.

3. A large-scale specimen fatigue crack growth test procedure was considered as a reference for a second validation case. The 3D FE modeling procedure was used to reproduce the three cracks that were initiated and monitored consecutively in the experiment. Discrepancies between the experimental measurements and numerical solutions were addressed through a deterministic material variation and misalignment study.

5 Conclusion

A two-degree of freedom analytical model was numerically implemented in MATLAB for three different elliptical cracks (surface, embedded and corner) under nominal tensile loading conditions. Results generated through the 3D FEA based method with identical load conditions and initial crack geometry were verified against analytical solutions. Datasets generated by the two models were found to be in very good agreement with each other, presenting similar crack front shape evolution and fatigue lives. Minimal differences in crack shape evolution were explained by accuracy limitations and simplified crack front definition of the analytical model, and the absence thereof in the FEA package.

Two sets of experimental measurements available in the literature were used as a reference in a modeling validation study. The two datasets were based on two specimen configurations containing five notches (to initiate fatigue cracks) and subjected to uniform tensile loads Each test procedure configuration (specimen geometry, far field loading, initial flaw size) was represented digitally in the 3D FE model. Crack propagation trajectory for the five cracks in each of the specimen configurations shows to be in good agreement with the experimental results. Furthermore, the predicted fatigue life of each specimen was quite accurate given the complex interaction that exist between the five cracks that grow simultaneously.

As part of a life extension program for the A-10 Thunderbolt II a full-sized spar was subjected to three separate fatigue crack growth tests. In order to validate the 3D FEA methodology at the large-scale specimen level, a simplified model was defined. Static analysis was performed to confirm that the stress distribution and overall behaviour under tensile loads was representative to the fully detailed spar. Nominal boundary conditions, material properties and loads were used for the initial phase of the validation process. The numerical results matched well the experimental data for the first crack, however, numerical solutions for second and third crack did not match the experimental measurement. A detailed study was performed to explain possible causes for the mismatch. It was concluded that a off-nominal loading conditions of the spar in the testing rig and fatigue crack growth rate scatter associated with the material represent sources of experimental uncertainty that have to be considered in the validation process. A series of simulations were

performed to characterize the effect of material properties and load applications at the end of which the experimental results were reproduced with the proposed FEA modelling approach.
The 3D FEA based method proved to be both accurate and efficient in assessing remaining useful life and crack paths for simple and complex geometric representations of test coupons.

5.1 Future Recommendations

The deterministic nature of the models used for this research, although useful to characterize material behaviour for specific material and test conditions, do not account for potential variations that could affect crack growth rate, fatigue life and/or crack path. Probabilistic analysis, such as Monte Carlo simulations, could provide a better behavioural understanding of the components analyzed by accounting for the statistical nature of material properties and operating conditions.

It was noted that some of the test conditions parameters were not known with high confidence for each stage of the experiment. A more complete set of data gathering tools should be used in fatigue crack growth testing of full-sized components. Strain measurements should be taken throughout the experiment in order to confirm proper alignment of the part, especially for large items, and not only during the preliminary stages of test campaigns.

6 Bibliography

[1] W. Rankine, "On the Causes of the Unexpected Breakage of the Journals of Railway Axles; And on the Means of Preventing Such Accidents by Observing the Law of Continuity in Their Construction," *Journal of the Franklin Institute,* vol. 36, no. 3, pp. 178-180, 1843.

[2] W. Schutz, "A history of fatigue," *Engineering Fracture Mechanics,* vol. 54, no. 2, pp. 263-300, 1996.

[3] T. L. Anderson, Fracture Mechanics: Fundamentals and Application, 3 ed., Boca Raton: CRC Taylor & Francis, 2005.

[4] J. R. Gebman, "Challenges and Issues with the Further Aging of U.S. Air Force Aircraft," RAND Corporation, Santa Monica, 2009.

[5] R. Davies and D. Birtles., "Comet: The World's First Jet Airliner.," McLean, Virginia, 1999.

[6] P. A. Withey, "Fatigue Failure of the de Havilland Comet I, Engineering 9 Failure Analysis," *Engineering Failure Analysis,* vol. 4, no. 2, pp. 147-154, 1997.

[7] C. F. Tiffany, J. P. Gallagher and C. A. Babish, "Threats to Aircraft Structural Safety, Including A Compendium of Selected Structural Accidents / Incidents," Air Force Flight Dynamics Laboratory, Wright-Patterson Air Force Base, Dayton, 2010.

[8] R. Wanhill, L. Molent and S. Barter, "Milestone Case Histories in Aircraft Structural Integrity," National Aerospace Laboratory NLR (Netherlands) and Defence Science and Technology Group DSTG (Australia), 2021.

[9] G. Negaard, "The History of the Aircraft Structural Integrity Program," Air Force Flight Dynamics Laboratory, Wright-Patterson Air Force Base, Dayton, 1980.

[10] U. G. Goranson, "Damage Tolerance Facts and Fiction," in *International Conference on Damage Tolerance of Aircraft Structures*, Delft, 2007.

[11] G. Irwin, "Onset of Fast Crack Propagation in High Strength Steel and Aluminum Alloys," in *Sagamore Research Conference Proceedings*, 1956.

[12] G. Irwin, "Analysis of Stresses and Strains near the End of a Crack Traversing a Plate," *Journal of Applied Mechanics,* vol. 24, pp. 361-364, 1957.

[13] A. Griffith, "The phenomena of rupture and flow in solids," *Royal Soc. London,* vol. 221, pp. 163-198, 1921.

[14] S. Yarema, "On the contribution of G. R. Irwin to fracture mechanics," *Mater Sci,* vol. 31, pp. 617-623, 1996.

[15] D. Lutz and P. C. Paris, "Pioneer of fracture mechanics, honored for his work," *The Source,* 2010.

[16] P. Paris, M. Gomez and W. Anderson, "A Rational Analytic Theory of Fatigue," *he Trend in Engineering,* vol. 13, pp. 9-14, 1961.

[17] SWRI., "NASGRO: Fracture Mechanics and Fatigue Crack Growth Analysis Software," Southwest Research Institute, 2021.

[18] LEXTECH., "AFGROW: Fracture Mechanics and Fatigue Crack Growth Analysis Software Tool," LexTech, Inc., Centerville, 2021.

[19] R. Forman and S. Mettu, "Behavior of Surface and Corner Cracks Subjected to Tensile and Bending Loads in Ti – 6Al – 4V Alloy," *ASTM STP 1131, American Society for Testing and Materials,* pp. 519-546, 1992.

[20] S. R. Mettu, "NASGRO 3.0 – A Software for Analyzing Aging Aircraft," in *The Second Joint NASA/FAA/DoD Conference on Aging Aircraft*, 1999.

[21] A. Koernig and N. Andersson, "Thermo-mechanical fatigue crack propagation in single-crystal turbine blade," Linkoping University, 2016.

[22] N. E. Dowling, Mechanical Behaviour of Materials, Engineering Methods for Deformation, Fracture and Fatigue, 4 ed., Pearson.

[23] G. Glinka and G. Shen, "Universal features of weight functions for cracks in Mode I," *Engineering Fracture Mechanics,* vol. 40, no. 6, pp. 1135-1146, 1991.

[24] L. Tang, A. Ince and J. Zheng, "Numerical modeling of residual stresses and fatigue damage assessment of ultrasonic impact treated 304L stainless steel welded joints," *Engineering Failure Analysis,* vol. 108, 2020, 104277.

[25] D. Parks, "A stiffness derivative finite element technique for determination of crack tip stress intensity factors," *Int J Fract,* vol. 10, no. 4, pp. 487-502, 1974.

[26] J. Rice, "A path independent integral and the approximate analysis of strain concentration by notches and cracks," *J Appl Mech,* vol. 35, pp. 379-386, 1968.

[27] D. Tracey, "Finite elements for determination of crack tip elastic stress intensity factors," *Eng. Frac. Mech.,* vol. 3, pp. 255-265, 1971.

[28] D. Tracey, "Discussion of ‘on the use of isoparametric finite elements in linear fracture mechanics’," *Int J Numer Meth Engng,* vol. 11, no. 2, pp. 401-402, 1977.

[29] R. Branco, F. Antunes and J. Costa, "A review of 3D-FE adaptive remeshing techniques for crack growth modelling," *Engineering Fracture Mechanics,* vol. 141, pp. 170-195, 2015.

[30] N. Moes, J. Dolbow and B. T., "A finite element method for crack growth without remeshing," *International Journal for Numerical Methods in Engineering,* vol. 46, pp. 131-150, 1999.

[31] N. Moës, A. Gravouil and T. Belytschko, "Non-planar 3d crack growth by the extended finite element and level sets-part I: mechanical model: non-planar 3d crack growth," *International Journal for Numerical Methods in Engineering,* 2002.

[32] J. Newman. and I. Raju, "Stress-Intensity Factor Equations for Cracks in Three-Dimensional Finite Bodies Subjected to Tension and Bending Loads," NASA TM 85793, 1984.

[33] A. Fatemi and N. Shamsaei, "Multiaxial fatigue: an overview and some approximation models for life estimation," *Int. J. Fatigue,* vol. 33, pp. 948-958, 2011.

[34] G. R. Irwin, "The Crack Extension Force for a Part-Through Crack in a Place," *J. Appl. Mech.,* vol. 29, no. 4, pp. 651-654, 1962.

[35] F. V. Smith, A. F. Emery and A. S. Kobayashi, "Stress Intensity Factors for Semi-Circular Cracks, Part 2 – Semi-infinite Solid," *J. Appl. Mechs.,* vol. 34, no. 4, 1967.

[36] I. Raju and J. Newman, "Stress-Intensity Factors for a Wide Range of Semi-Elliptical Surface Cracks in Finite-Thickness Plates," *Engineering Fracture Mechanics,* vol. 11, no. 4, pp. 817-829, 1979.

[37] I. Heliot, L. R. and A. Pellissier-Tanon, "Benchmark Problems No. 1 - Semi-Elliptical Surface Crack," *Int. J. of Fracture,* vol. 15, no. 6, pp. 197-202, 1979.

[38] S. A. Fawaz and B. Anderson, *Eng. Fract. Mech.,* vol. 71, pp. 1235-1254, 2004.

[39] Y. Bombardier and M. Liao, "Paper AIAA 2010-2864," in *1st AIAA/ASME/ASCE/AHS/ASC SDM Conference*, 2010.

[40] I. Raju and J. Newman, "Stress Intensity Factors for Corner Cracks in Rectangular Bars," in *Fracture Mechanics: Nineteenth Symposium*, Philadelphia, 1988.

[41] J. Kim, T. Chau-Dinh, G. Zi, W. W. Lee and J. S. Kong, "Probabilistic fatigue integrity assessment in multiple crack growth analysis associated with equivalent initial flaw and material variability," *Engineering Fracture Mechanics,* vol. 156, pp. 182-196, 2016.

[42] R. E. Heller, "Damage Tolerance Predictions for Spar Web Cracking In A Diminishing Stress Field," Department of Mechanical Engineering, University of Utah, A-10 Systems Program Office Hill AFB Utah, 2011.

[43] A. Ince, "Computational crack propagation modeling of welded structures under as-welded and ultrasonic impact treatment conditions," *Fatigue & Fracture of Engineering Materials & Structures,* vol. 45, no. 2, pp. 578-592, 2022.

[44] B. D. Fehl and Z. K. Truman, "An evaluation of fracture mechanics quarter-point displacement techniques used for computing stress intensity factors," *Engineering Structures,* vol. 21, pp. 406-415, 1999.

[45] F. Erdogan and G. C. Sih, "On the Crack Extension in Plates under Plane Loading and Transverse Shear," *Journal of Basic Engineering,* vol. 85, pp. 519-525, 1963.

[46] S. Glodez, M. Sraml and J. Kramberger, "A computational model for determination of service life of gears," *Int. J. Fatigue,* vol. 24, pp. 1013-1020, 2002.

[47] R. Barsoum, "On the use of isoparametric finite elements in linear fracture mechanics*," *International Journal for Numerical Methods In Engineering,* vol. 10, pp. 25-37, 1976.

[48] A. Ingraffea and C. Manu, "Stress-Intensity Factor Computation in Three Dimensions With Quarter-Point Elements," *International Journal For Numerical Methods In Engineering,* vol. 15, pp. 1427-1445, 1980.

[49] P. C. Ilie, A. Ince and A. Loghin, "Assessment of fatigue crack growth based on 3D finite element modeling approach," *Procedia Structural Integrity,* vol. 38, pp. 271-282, 2021.

[50] F. W. Smith and M. J. Alavi, "Stress intensity factors for a penny shaped crack in a half space," *Engng Fracture Mech.,* vol. 3, no. 3, pp. 241-254, 1971.

[51] F. W. Smith and D. R. Sorensen, "Mixed mode stress intensity factors for semi-elliptical surface cracks," NASA CR-134684, 1974.

[52] A. S. Kobayashi, N. Polvanich, A. F. Emery and W. J. Love, "Surface flaws in a plate in bending.," in *Proc. 12th Annual Meeting Soc Engng Sci.*, Austin, 1975.

[53] A. S. Kobayashi and A. N. Enetanya, "Stress-Intensity Factor of a Cornier Crack," *Mechanics of Crack Growth,* pp. 477-495, 1976.

[54] SWRI., "NASGRO 3.0, Appendix A, Material Constants," Southwest Research Institute, San Antonio.

[55] ANSYS®, "Help System, Mechanical APDL Theory Reference," ANSYS, Inc..

[56] J. C. Newman, E. P. Phillips and A. Everett R., "Fatigue analyses under constant and variable amplitude loading using small-crack theory," NASA TM-1999-209329, 2001.

[57] C. Annis, "Probabilistic Life Prediction Isn't as Easy as It Looks," *Probabilistic Aspects of Life Prediction ASTM STP-1450,* 2003.